

1 Source attribution of black carbon and its direct radiative forcing
2 in China

3
4
5
6 Yang Yang¹, Hailong Wang^{1*}, Steven J. Smith², Po-Lun Ma¹, Philip J. Rasch¹

7
8
9
10 ¹Atmospheric Science and Global Change Division, Pacific Northwest National
11 Laboratory, Richland, Washington, USA

12 ²Joint Global Change Research Institute, Pacific Northwest National Laboratory,
13 College Park, Maryland, USA

14
15
16 *Correspondence to yang.yang@pnnl.gov and hailong.wang@pnnl.gov

18 **Abstract**

19 The source attributions for mass concentration, haze formation, transport, and
20 direct radiative forcing of black carbon (BC) in various regions of China are quantified
21 in this study using the Community Earth System Model (CESM) with a source-tagging
22 technique. Anthropogenic emissions are from the Community Emissions Data
23 System that is newly developed for the Coupled Model Intercomparison Project
24 Phase 6 (CMIP6). Over North China where the air quality is often poor, about 90% of
25 near-surface BC concentration is contributed by local emissions. 30% of BC
26 concentration over South China in winter can be attributed to emissions from North
27 China and 10% comes from sources outside China in spring. For other regions in
28 China, BC is largely contributed from non-local sources. We further investigated
29 potential factors that contribute to the poor air quality in China. During polluted days,
30 a net inflow of BC transported from non-local source regions associated with
31 anomalous winds plays an important role in increasing local BC concentrations.
32 BC-containing particles emitted from East Asia can also be transported across the
33 Pacific. Our model results show that emissions from inside and outside China are
34 equally important for the BC outflow from East Asia, while emissions from China
35 account for 7% of BC concentration and 25% in column burden in western United
36 States in spring. Radiative forcing estimated shows that 66% of the annual mean BC
37 direct radiative forcing (2.3 W m^{-2}) in China results from local emissions, and the
38 remaining 34% are contributed by emissions outside of China. Efficiency analysis
39 shows that reduction in BC emissions over eastern China could benefit more on the
40 regional air quality in China, especially in winter haze season.

41 **1. Introduction**

42 Black carbon (BC), as a component of atmospheric fine particulate matter
43 (PM_{2.5}), is harmful to human health (Anenberg et al., 2011; Janssen et al., 2012). In
44 addition to its impact on air quality, as the most efficient light-absorbing
45 anthropogenic aerosols, BC is thought to exert a substantial influence on climate
46 (Bond et al., 2013; IPCC, 2013; Liao et al., 2015). It can heat the atmosphere through
47 absorbing solar radiation (Ramanathan and Carmichael, 2008), influence cloud
48 microphysical and dynamical processes (Jacobson, 2006; McFarquhar and Wang,
49 2006), and reduce surface albedo through deposition on snow and ice (Flanner et al.,
50 2007; Qian et al., 2015).

51 Due to accelerated urbanization and rapid economic growth, emissions of BC in
52 China increased dramatically during recent decades. It contributed to about one
53 fourth of the global emissions of BC in recent decades (Bond et al., 2007). Strong
54 emissions lead to high concentrations of BC over China. Zhang et al. (2008) collected
55 aerosol samples at eighteen stations spread over China during 2006 and reported BC
56 concentrations in a range of 9–14 $\mu\text{g m}^{-3}$ at urban sites, 2–5 $\mu\text{g m}^{-3}$ at rural sites, and
57 about 0.35 $\mu\text{g m}^{-3}$ at remote background sites. BC also exerts significant positive
58 direct radiative forcing (DRF) at the top of the atmosphere (TOA) in China. Using the
59 Regional Climate Chemistry Modeling System (RegCCMs), Zhuang et al. (2013)
60 reported an annual mean BC DRF of 2–5 W m^{-2} at TOA over eastern China and
61 about 6 W m^{-2} over Sichuan Basin in year 2006. Li et al. (2016) also showed a strong
62 DRF of BC over the North China Plain and Sichuan Basin in most seasons except for
63 spring when the strongest BC DRF with values of 4–6 W m^{-2} shifted to southern
64 China.

65 BC is the product of incomplete combustion of fossil fuels, biofuels, and open
66 burning, such as forest and grassland fires and agricultural waste burning on fields. In
67 the atmosphere the average lifetime of BC is only a few days, due to both wet
68 removal and dry deposition, which is much shorter than that of long-lived greenhouse
69 gases. In addition, BC lifetime is region dependent. BC in East Asia has a shorter
70 lifetime than the global mean value due to a faster regional removal (H. Wang et al.,

71 2014), probably associated with strong precipitation during monsoon season. BC
72 emission reductions may benefit both mitigation of global climate change and
73 regional air quality (Shindell et al., 2012; Bond et al., 2013; Smith and Mizrahi, 2013),
74 especially in East Asia where fuel combustion emits substantial BC along with other
75 pollutant species. Many previous observational and/or modeling studies have
76 examined the source sector contributions of BC over China (Zhuang et al., 2014;
77 Y.-L. Zhang et al., 2015; Li et al., 2016). They found that residential heating and
78 industry sectors were the largest contributors to BC concentrations in China, while
79 biomass burning emissions from outside China were important to BC in western
80 China. An effective BC reduction in a receptor region would require knowing not only
81 the source sector that contributes the most to BC levels, but also the source
82 contributions from various locations within and outside the region. However, very few
83 previous studies have focused on the source attribution of BC concentrations in
84 various regions of China. Li et al. (2016) examined the contributions of emissions
85 inside and outside China to BC over China (with only two source regions) but did not
86 divide the source contributions from different regions inside China.

87 Pollution levels also show substantial daily to weekly variation. In recent years,
88 extreme wintertime hazy conditions occurred frequently in China and caused serious
89 air pollution, affecting more than half of the 1.3 billion people (Ding and Liu, 2014).
90 During one winter haze episode in 2013, BC concentrations increased up to about 20
91 and $8 \mu\text{g m}^{-3}$ in Xi'an and Beijing over northern China, and 6 and $4 \mu\text{g m}^{-3}$ in
92 Guangzhou and Shanghai over southern China, respectively (Y.-L. Zhang et al.,
93 2015). The transport of pollutants from upwind was reported to be one of the most
94 important contributors to local high aerosol concentrations during haze days (L. T.
95 Wang et al., 2014; Y. Yang et al., 2016). L. T. Wang et al. (2014) found that emissions
96 from northern Hebei and Beijing-Tianjin were the major contributor to particulate
97 matter ($\text{PM}_{2.5}$) pollution in Shijiazhuang in January 2013. Yang et al. (2016) confirmed
98 a connection between wind fields and $\text{PM}_{2.5}$ concentrations during winter hazy days
99 through model simulations and statistical analysis. They also found that weakened
100 winds contributed to increases in winter aerosol concentrations and hazy days over

101 eastern China during recent decades. As a chemically inert species, atmospheric BC
102 is a good tracer to investigate the source region contributions from local and non-local
103 emissions during polluted conditions that are related to long-range transport.

104 BC particles originating from East Asia can also be transported across the North
105 Pacific, reaching North America (Hadley et al., 2007; Ma et al., 2013a; Matsui et al.,
106 2013; H. Wang et al., 2014; Yang et al., 2015). Matsui et al. (2013) simulated outflow
107 of BC from East Asia using the Community Multiscale Air Quality (CMAQ) model and
108 found that anthropogenic emissions from China, biomass burning emissions from
109 Southeast Asia, and biomass burning emissions from Siberia and Kazakhstan
110 contributed 61%, 17%, and 6%, respectively, to the eastward BC flux at 150°E
111 averaged over 2008–2010. Hadley et al. (2007) estimated the trans-Pacific transport
112 of BC during April of 2004 using the Chemical Weather Forecast System (CFORS)
113 model and reported that, across 130°W, 75% of BC transported into North America
114 originated from Asia. Huang et al. (2012) simulated BC using the Sulfur Transport
115 and Deposition Model (STEM), and found emissions outside North America
116 contributed to 30–80% of column BC over North America in summer 2008. H. Wang
117 et al. (2014) examined the long-term (1995–2005) average global source-receptor
118 relationship of BC and found that BC emitted from the entire East Asia only contribute
119 less than 5% to the total BC burden in North America, although the contribution is up
120 to 40% near the west coast region. Few studies have examined the outflow from East
121 Asia and inflow into North America contributed from source regions in and outside
122 China. In addition, the emissions of BC from China increased dramatically during the
123 last few years, with the annual total anthropogenic emissions estimated to have
124 almost doubled in year 2014 compared to year 2000, shown in the newly developed
125 Community Emissions Data System (CEDS; Hoesly et al. 2017). Therefore, the
126 long-range transport of BC and source-receptor relationships could be quite different
127 from previous studies.

128 Due to its warming effect in the climate system, BC is potentially important for
129 climate mitigation and has drawn much attention recently. Source attribution of the
130 direct radiative effect of BC is likely to be different from that of near-surface

131 concentration and column burden due to the dependence of radiative forcing on the
132 vertical distribution of BC and its mixing state with other species that are influenced
133 by different regional sources. In this study, we use the Community Earth System
134 Model (CESM) with improved representations of aerosol transport and wet removal
135 (H. Wang et al., 2013) and a BC source-tagging technique (H. Wang et al., 2014).
136 Anthropogenic emissions from the newly developed CEDS inventory (Hoesly et al.,
137 2017), as released for the Coupled Model Intercomparison Project Phase 6 (CMIP6),
138 are used to examine the source attributions for mass concentration, long-range
139 transport, and direct radiative forcing of BC in various regions of China. We aim to
140 quantify: (1) source region contributions to concentrations of BC over various
141 receptor regions in China; (2) contributions to changes in BC concentrations under
142 polluted conditions; (3) source contributions to trans-boundary and trans-Pacific
143 transport of BC; and (4) source contributions to direct radiative forcing of BC in China.

144 The CESM model, emissions, and numerical experiment are described in
145 Section 2. Section 3 provides evaluation of the simulated concentration and aerosol
146 absorption optical depth of BC in China. Section 4 investigates source contributions
147 to near-surface concentrations, long-range transport and direct radiative forcing of BC
148 over various receptor regions using the BC source-tagging technique in CESM.
149 Section 5 summarizes these results.

150

151 **2. Methods**

152 We simulate the evolution and direct radiative forcing (DRF) of BC using CESM
153 version 1.2 (Hurrell et al., 2013). The atmospheric model in CESM is version 5 of the
154 Community Atmosphere Model (CAM5), with horizontal grid spacing of 1.9° latitude
155 by 2.5° longitude and 30 vertical layers ranging from the surface to 3.6 hPa used in
156 this study. The model treats the properties and processes of major aerosol species
157 (sea salt, mineral dust, sulfate, black carbon, primary organic matter and secondary
158 organic aerosol) using a three-mode modal aerosol module (MAM3), in which aerosol
159 size distributions are represented by three lognormal modes: Aitken, accumulation,
160 and coarse modes. BC is emitted to the accumulation mode. Mass mixing ratios of

161 different aerosol species and the number mixing ratio are predicted for each mode. A
162 more detailed description of the MAM3 representation can be found in Liu et al.
163 (2012). Aerosol dry deposition velocities are calculated using the Zhang et al. (2001)
164 parameterization. The wet deposition of aerosols in our CAM5 model includes
165 in-cloud wet removal (i.e., activation of interstitial aerosols to cloud-borne particles
166 followed by precipitation scavenging) and below-cloud wet removal (i.e., capture of
167 interstitial aerosol particles by falling precipitation particles) for both stratiform and
168 convective clouds. Aerosol activation is calculated with the parameterization of
169 Abdul-Razzak and Ghan (2000) for stratiform cloud throughout the column and
170 convective cloud at cloud base, while the secondary activation above convective
171 cloud base has a simpler treatment with an assumed maximum supersaturation in
172 convective updrafts (H. Wang et al., 2013). The unified treatment for convective
173 transport and aerosol wet removal along with the explicit aerosol activation above
174 convective cloud base was developed by H. Wang et al. (2013) and included in the
175 CAM5 version being used in this study. This implementation reduces the excessive
176 BC aloft and better simulates observed BC concentrations in the mid- to
177 upper-troposphere. Aerosol optical properties for each mode are parameterized
178 according to Ghan and Zaveri (2007). Refractive indices for aerosols are taken from
179 the OPAC (optical properties for aerosols and clouds) software package (Koepke and
180 Schult, 1998), but for BC at solar wavelengths the values are updated from Bond and
181 Bergstrom (2006). In MAM3, the aging process of BC is neglected by assuming the
182 immediate mixing of BC with other aerosol species. Direct radiative forcing of BC is
183 calculated as the difference in the top-of-the-atmosphere net radiative fluxes with and
184 without BC for the all-sky condition following Ghan (2013).

185 Anthropogenic emissions used in this study are from the CEDS dataset, as
186 released for the CMIP6 model experiments (Hoesly et al. 2017). This newly released
187 emission inventory includes aerosol (black carbon, organic carbon) and aerosol
188 precursor and reactive compounds (sulfur dioxide, nitrogen oxides, ammonia, carbon
189 monoxide, and non-methane volatile organic compounds). The emissions are
190 provided at monthly resolution for each year of 1750–2014 on a $0.5^\circ \times 0.5^\circ$ grid and

191 include agricultural, energy, industry, residential, international shipping, solvents,
192 surface transportation, waste treatment, and aircraft sectors. The biomass burning
193 emissions used in this study are also developed for CMIP6 based on Global Fire
194 Emission Database (GFED) version 4, Fire Model Intercomparison Project (FireMIP),
195 visibility-observations and Global Charcoal Database (GCD) data (van Marle et al.
196 2016).

197 Figure 1a shows the horizontal spatial distribution of annual emissions of BC
198 averaged over the most recent 5 years (2010–2014) and the seven geographical
199 source regions tagged in continental China, including North China (NC), South China
200 (SC), Southwest China (SW), Central-West China (CW), Northeast China (NE),
201 Northwest China (NW), and Tibetan Plateau (TP). Figure 1b summarizes the total
202 seasonal BC emissions in each of these source regions. North China has the largest
203 annual emissions of BC in China, with maximum emission larger than 1.2 g C m^{-2}
204 year^{-1} and a regional total emission of $1089 \text{ Gg C year}^{-1}$ (44% of total emissions from
205 continental China). Annual emissions of BC also have large values over South and
206 Southwest China, with maximum values in the range of $0.8\text{--}1.2 \text{ g C m}^{-2} \text{ year}^{-1}$,
207 followed by Central-West and Northeast China. Over the less economically
208 developed Northwest China and remote region Tibetan Plateau, emissions of BC are
209 much lower than other regions in China. The seasonal mean emissions of BC also
210 show the same spatial pattern as the annual means. BC had the largest emissions
211 over North, South, and Southwest China in all seasons, among which emissions are
212 strongest in December-January-February (DJF), especially over North China,
213 resulting from domestic heating. The total seasonal emissions of BC in continental
214 China are 797, 586, 537, and 577 Gg C in DJF, March-April-May (MAM),
215 June-July-August (JJA), and September-October-November (SON), respectively,
216 which add up to a total annual BC emissions of 2497 Gg C averaged over years
217 2010–2014. The anthropogenic emissions of BC in China in 2010–2014 are larger
218 than those used in the previous studies for earlier years (Table S1), partly as a result
219 of a higher estimate of BC emissions from coal coking production. The higher
220 emissions likely lead to higher concentrations and direct radiative forcing, and source

221 contributions of BC in China, compared to the values reported in these studies. The
222 DJF emissions account for 26–35% of annual total whereas emissions in JJA only
223 account for 17–24% over the seven source regions in continental China. Total BC
224 emissions from neighboring regions including rest of East Asia (REA, with China
225 excluded), South Asia (SAS), Southeast Asia (SEA), and Russia/Belarusia/Ukraine
226 (RBU) are shown in Figure 1c. These source regions outside China are consistent
227 with source regions defined in the second phase of Hemispheric Transport of Air
228 Pollution (HTAP2). South Asia and Southeast Asia have relatively high emissions.
229 They may dominate the contribution to concentrations and direct radiative forcing of
230 BC in China, especially southern and western China, from foreign sources through
231 long-range transport.

232 An explicit BC source tagging capability was originally implemented in CAM5 by
233 H. Wang et al. (2014), through which emissions of BC from independent source
234 regions and/or sectors can be explicitly tracked. This method quantifies the source–
235 receptor relationships of BC in any receptor region within a single model simulation
236 without perturbing emissions from individual source regions or sectors. R. Zhang et
237 al. (2015a,b) used this method to quantify the source attributions of BC in western
238 North America, Himalayas, and Tibetan Plateau. The same BC source tagging
239 technique is implemented to a newer model version (CAM5.3) and applied in this
240 study to quantify the source attributions of concentration, transport and direct
241 radiative forcing of BC in various regions of China. BC emissions (anthropogenic plus
242 biomass burning) from seven geographical source regions, including North China,
243 South China, Southwest China, Central-West China, Northeast China, Northwest
244 China, Tibetan Plateau in China, and from rest of the world (RW) are tagged.
245 Transport and physics tendencies are calculated separately for each tagged BC in
246 the same way as the original BC simulation in CESM. We choose the seven individual
247 regions (North China, South China, Southwest China, Central-West China, Northeast
248 China, Northwest China, and Tibetan Plateau) and all seven regions combined
249 (hereafter continental China) as receptor regions in this study to examine the
250 source-receptor relationships of BC. While all emissions, including sulfur dioxides,

251 organic carbon and BC, were used in the model simulation, tagging was only applied
252 to BC emissions.

253 The CAM5 simulation is performed at $1.9^\circ \times 2.5^\circ$ horizontal grid spacing using the
254 specified-dynamics mode (Ma et al., 2013b), in which large-scale circulations (i.e.,
255 horizontal winds) are nudged to 6-hourly reanalysis data from the Modern Era
256 Retrospective-Analysis for Research and Applications (MERRA) reanalysis data set
257 (Rienecker et al., 2011) with a relaxation time scale of 6 hours (K. Zhang et al., 2014).
258 The use of nudged winds allows for a more accurate simulation so that the key role of
259 large-scale circulation patterns matches observations over the specified years. The
260 simulation is run from year 2009 to 2014, with both time-varying aerosol emissions
261 and meteorological fields. The first year is for spin-up and the last five years are used
262 for analysis.

263

264 **3. Model evaluation**

265 The simulations of aerosols, especially BC, using CAM5 have been extensively
266 evaluated against observations including aerosol mass and number concentrations,
267 vertical profiles, aerosol optical properties, aerosol deposition, and cloud-nucleating
268 properties in several previous studies (e.g., Liu et al., 2012, 2016; H. Wang et al.,
269 2013; Ma et al., 2013b; Jiao et al., 2014; Qian et al., 2014; R. Zhang et al., 2015a,b).
270 Here we focus on the evaluation of model performance in China using measurements
271 of near-surface BC concentrations, vertical profiles, aerosol index derived from
272 satellite, and aerosol absorption optical depth from the Aerosol Robotic Network
273 (AERONET).

274 **3.1 Mass concentrations and column burden of BC**

275 Figure 2 presents spatial distributions of simulated seasonal mean near-surface
276 concentrations and column burden of BC, both of which show a similar spatial pattern
277 to emissions of BC (Figure 1a) with the largest values over North China and the
278 lowest values over Northwest China and Tibetan Plateau. Near-surface model results
279 are taken to be the lowest model layer (from surface to 985 hPa in average). Among
280 all seasons, DJF has the highest BC levels, with values in the range of 6–12, 2–8,

281 and $1\text{--}8\ \mu\text{g m}^{-3}$ for near-surface concentrations and $5\text{--}9$, $3\text{--}7$, $2\text{--}9\ \text{mg m}^{-2}$ for column
282 burden over North, South, and Southwest China, respectively. In contrast, JJA has
283 the lowest BC concentrations over China due to the lower emissions and larger wet
284 scavenging associated with East Asian summer monsoon (Lou et al., 2016).
285 Averaged over continental China, near-surface BC concentrations are 2.2, 1.1, 0.8,
286 and $1.3\ \mu\text{g m}^{-3}$ in DJF, MAM, JJA, and SON, respectively, with seasonal variability of
287 38%. The column burden of BC shows smaller seasonal variability (26%), with
288 area-weighted average of 1.9, 1.4, 1.1, and $1.3\ \text{mg m}^{-2}$ in DJF, MAM, JJA, and SON,
289 respectively, in China. The magnitude, spatial distribution, and seasonal variations of
290 simulated near-surface BC concentrations over China are similar to those in Fu et al.
291 (2012) and X. Wang et al. (2013) using Intercontinental Chemical Transport
292 Experiment-Phase B (INTEX-B) emission inventory (Zhang et al., 2009) and those in
293 Li et al. (2016) using HTAP emission inventory (Janssens-Maenhout et al., 2015)
294 together with a global chemical transport model.

295 The simulated near-surface BC concentrations are evaluated here using
296 measurements at fourteen sites of the China Meteorological Administration
297 Atmosphere Watch Network (CAWNET) (Zhang et al., 2012). The locations of
298 CAWNET sites are shown in Figure S1a. The observational data include monthly BC
299 concentrations in years 2006–2007. Note that the simulated BC concentrations are
300 for years 2010–2014. Figure 3a compares the simulated seasonal mean near-surface
301 BC concentrations with those from CAWNET observations and Table S2 summarizes
302 the comparison in different regions, using modeled values from the grid cell
303 containing each observational site. Simulated BC concentrations at most sites are
304 within the range of one third to three times of observed values, except for Dunhuang
305 (94.68°E , 40.15°N) and Lhasa (91.13°E , 29.67°N) sites over western China, where
306 BC concentrations appear to be underestimated in the model (up to 20 times lower).
307 The possible bias is discussed in the following part. Over North China, simulated
308 concentrations are similar to observations in DJF, but underestimated in other
309 seasons. Over South China, the simulations do not have large biases compared to
310 the observed BC. However, simulated BC is underestimated in all seasons over

311 Southwest, Central-West, Northeast, Northwest China, and Tibetan Plateau.
312 Compared to the CAWNET data, the modeled near-surface BC concentrations have
313 a normalized mean bias (NMB) of -53% . Note that anthropogenic BC emissions went
314 up by a factor of 1.18 between 2006–2007 and 2010–2014. An emissions adjusted
315 comparison would result in an even larger underestimation. There are several
316 reasons that might cause low bias in this comparison. Liu et al. (2012) and H. Wang
317 et al. (2013) have previously found underestimation of BC concentrations over China
318 in CAM5 model and suggested the BC emissions may be significantly
319 underestimated. Using the global chemical transport model GEOS-Chem together
320 with emissions in 2006, Fu et al. (2012) found the simulated BC concentrations in
321 China were underestimated by 56%. With HTAP emissions at the year 2010 level, Li
322 et al. (2016) showed a low bias of 37% in simulated BC concentration in China.
323 Larger wet removal rate and shorter lifetime of aerosols along with the instantaneous
324 aging of BC in the MAM3 can also lead to the lower concentrations of BC (e.g., Wang
325 et al., 2011; Liu et al., 2012; H. Wang et al., 2013; Kristiansen et al., 2016).

326 Another potential cause for a bias in this comparison is spatial sampling bias.
327 Half of the CAWNET sites are located in urban areas, which will tend to have high
328 values near sources, whereas the modeled values represent averages over large grid
329 cells (R. Wang et al., 2014), as further discussed below.

330 The model captures well the spatial distribution and seasonal variation of BC
331 concentrations in China, having a statistically significant correlation coefficient of
332 $+0.58$ between simulated and observed seasonal BC concentrations over CAWNET
333 sites.

334 Figure S2 compares the observed and simulated vertical profiles of BC
335 concentrations in the East-Asian outflow region. The model successfully reproduces
336 the vertical profile of BC that was measured in March–April 2009 during the
337 A-FORCE field campaign and reported by Oshima et al. (2012).

338 **3.2 Aerosol absorption optical depth of BC**

339 To evaluate the simulated aerosol absorption optical depth (AAOD) of BC, the
340 AAOD data from AERONET (Holben et al., 2001) are used here. The locations of

341 AERONET sites in China are shown in Figure S1b. The observed AAOD are
342 averaged over years of 2010–2014 over seven sites and 2005–2010 over three sites
343 with data available. Most AERONET sites are over eastern and central China. AAOD
344 of BC at 550nm are calculated by interpolating AAOD at 440 and 675 nm and
345 removing AAOD of dust from the retrieved AERONET AAOD following Bond et al.
346 (2013). Figure 3b compares the observed and simulated seasonal mean AAOD of BC
347 at 550nm and Table S3 summarizes the comparisons in different regions. The model
348 has a low bias in simulating AAOD of BC in China, smaller than the bias in
349 near-surface concentrations, with a NMB of –16%. As is the case with surface
350 concentrations, this bias could be due to model issues, such as BC transport or
351 optical parameterization; an underestimate in emissions; or spatial sampling bias.
352 Simulated AAOD of BC are within the range of one third to three times of observed
353 values at most sites, with the spatial distribution and seasonal variation broadly
354 captured by the model. All but one of the observations are located in the North and
355 South China regions, and simulated BC AAOD are, on average, similar to
356 observations there. The AAOD from one observation site in Central-West China is
357 higher than the modeled value. Note that, the observed AAOD of BC is derived from
358 AERONET measurements using the absorption Ångström exponent. A recent study
359 (Schuster et al., 2016) reported that absorption Ångström exponent is not a robust
360 parameter for separating out carbonaceous absorption in the AERONET database,
361 which could cause biases in the AAOD estimates.

362 Figure 4 shows the spatial distribution of simulated seasonal mean AAOD of total
363 aerosols and Aerosol Index (AI) derived from Ozone Monitoring Instrument (OMI)
364 measurements over years of 2010–2014. AI is a measure of absorbing aerosols
365 including BC and dust. Compared to satellite AI data, the model roughly reproduces
366 spatial distribution of total AAOD in China, with large values over North, South, and
367 Southwest China in all seasons. AI derived from Total Ozone Mapping Spectrometer
368 (TOMS) measurements (Figure S3) also shows similar pattern as simulated AAOD. It
369 should be noted that, besides BC, dust particles also largely contribute to AI and
370 produces large AI values over Northwest China.

371 To examine the potential model bias more broadly we compared the difference of
372 AAOD and AI between western and eastern China (Fig. 4). Averaging AI and AAOD
373 broadly over eastern and western China, we find that AAOD/AI is 0.048 over eastern
374 China and 0.031 over western China. If we assume that the simulated AAOD do not
375 have large biases over eastern China based on the evaluation against observations
376 shown above (Fig. 3b and Table S3), then this difference hints a possible
377 underestimation of BC column burden in the model over the western regions.
378 However, it is difficult to draw a firm conclusion, given the likely differential role of dust
379 in eastern vs western China. This differential likely also contributes to AAOD biases in
380 modeling dust and may also impact biases in the satellite derived AI values.

381

382 **4. Source contributions to BC concentrations, transport and direct radiative** 383 **forcing**

384 **4.1. Source contributions to seasonal mean BC concentrations**

385 Figure 5 shows the simulated spatial distribution of seasonal near-surface BC
386 concentrations originating from the seven tagged source regions in continental China
387 and all other sources from outside China (rest of the world, RW) and Table S4
388 summarizes these source-receptor relationships. It is not surprising that regional
389 emissions largely influence BC concentrations in the same region. For example,
390 emissions of BC from North China give $5.8 \mu\text{g m}^{-3}$ of BC concentrations over North
391 China in DJF, whereas they only account for less than $1.3 \mu\text{g m}^{-3}$ over other regions
392 in China. However, the relatively small amount of BC from upwind source regions can
393 also be a large contributor to receptor regions near the strong sources. BC emissions
394 from North China contribute large amount to concentrations over South, Southwest,
395 Central-West, and Northeast China. BC emissions from South and Southwest China
396 also produce a widespread impact on BC over other neighboring regions. The
397 impacts of BC emitted from the remaining China regions are relatively small both in
398 local and non-local regions due to weak emissions (Fig. 1b). All the sources in China
399 have the largest impact in DJF, resulting from the strong BC emissions in winter,
400 while emissions from outside China have the largest impact on BC over China in

401 MAM due to the seasonal high emission over Southeast Asia and the strong
402 springtime southwesterly winds.

403 Averaged over continental China, emissions of BC from North China produce
404 mean BC concentrations of 0.4–1.1 $\mu\text{g m}^{-3}$, followed by 0.2–0.4 $\mu\text{g m}^{-3}$ from South
405 China and 0.1–0.2 $\mu\text{g m}^{-3}$ from Southwest China emissions. For emissions over
406 Central-West China, Northeast China, Northwest China, and Tibetan Plateau, their
407 individual impact is less than 0.15 $\mu\text{g m}^{-3}$. In contrast, emissions from outside China
408 result in 0.13 $\mu\text{g m}^{-3}$ of BC concentrations in China in MAM and less than 0.10 $\mu\text{g m}^{-3}$
409 in other seasons. The simulated source contributions to column burden of BC are
410 shown in Figure S4. They present a very similar spatial distribution and seasonal
411 variation to those of near-surface BC concentrations. However, the emissions from
412 outside China have a larger impact on the average column burden of BC over China
413 than on surface concentrations, with a magnitude of 0.5 mg m^{-2} in MAM, which is as
414 the same as that from sources in North China.

415 Figure 6 shows the spatial distribution of simulated relative contributions to
416 near-surface BC concentrations from sources in the seven regions in continental
417 China and those outside China by season. (The same plots for BC column burden are
418 shown in Figure S5.) For regions with higher emissions, their BC concentrations are
419 dominated by local emissions. In contrast, BC levels, especially column burden of
420 BC, over central and western China with lower emissions are strongly influenced by
421 non-local sources. Emissions from outside China can be the largest contributor to BC
422 over these regions. During DJF, MAM and SON, they contribute more than 70% to
423 both surface concentrations and column burden of BC in Tibetan Plateau, which is
424 important to the climate change due to the large climate efficacy of BC in snow (Qian
425 et al., 2011) and acceleration of snowmelt through elevated BC heat pump
426 mechanism (Lau et al., 2010). BC emissions from outside China also account for a
427 quite significant fraction of surface concentrations over Northwest and Southwest
428 China in MAM, which contribute to poor air quality over these regions.

429 Figure 7 summarizes source attribution for spatially averaged seasonal surface
430 BC concentrations for the seven receptor regions and continental China combined

431 (CN). Over North China, the majority of the BC concentrations are attributed to local
432 emissions in all seasons, with seasonal fractional contributions of 83–93%. Over
433 South China, the seasonal contributions from local emissions are in the range of 64–
434 87%. Emissions from North China account for 30% of BC concentrations over South
435 China in DJF, resulting from the wintertime northwesterly winds (Figure S6a), while
436 emissions from outside China contribute about 10% in MAM due to the strong
437 springtime biomass burning over southeast Asia and southwesterly winds
438 transporting BC from southeast Asia to South China (Figure S6b). Southwest China
439 has a similar level of local influence, with 59–79% of the BC concentration from local
440 emissions, whereas 17% are due to emissions from outside China transported by
441 westerly winds in MAM.

442 Non-local emissions from Southwest and North China contribute 27–49% of BC
443 concentration in Central-West China. North China emissions play an important role in
444 BC concentrations over Northeast China, with relative contributions in a range of 22–
445 36% in MAM, JJA and SON, while only 12% in DJF, which is associated with
446 northwesterly winds in winter preventing northward transport of BC from North China
447 to Northeast China. Over Northwest China and Tibetan Plateau, 22–40% and 43–
448 76%, respectively, of BC originate from emissions outside China due to the low
449 emissions over the less economically developed western China. For all of continental
450 China as the receptor, the seasonal BC concentrations are largely attributed to the
451 emissions from North and South China, with relative contributions ranging from 43–
452 50% and 18–24%, respectively, followed by contributions from Southwest China (10–
453 13%) and outside China (4–12%).

454 The source region contributions to column burden of BC in each receptor regions
455 in China are shown in Figure S7. In general, impacts on the non-local BC column
456 burden are larger than on surface concentrations because aerosol transport is
457 relatively easier in free-troposphere than in the boundary layer (e.g., Yang et al.,
458 2015). Column burdens of BC averaged over continental China mainly originate from
459 emissions in North China, South China and outside China, with relative contributions
460 ranging from 31–42%, 16–24% and 14–31%, respectively.

461

462 **4.2. Source contributions during polluted days**

463 Knowing the source attribution of BC during polluted days in China is important
464 for policy makers, which could provide an effective way for the mitigation of poor air
465 quality. Here, the polluted days are simply identified as days with daily concentrations
466 of BC higher than 90th percentile of probability density function in each receptor
467 regions. A total of different 45 days in winter in the 5-year simulation are identified as
468 polluted days for each region in China.

469 Figure 8 shows the DJF composite differences in near-surface BC concentrations
470 and winds at 850 hPa between polluted and normal days for each receptor region,
471 and Figure 9 summarizes the local and non-local source contributions to the
472 differences. When North China is under the polluted condition, BC concentrations are
473 higher by more than 70% compared to DJF average over North China, with a
474 maximum increase exceeding $5 \mu\text{g m}^{-3}$. North China local emissions contribute $5.4 \mu\text{g}$
475 m^{-3} to the averaged increase in BC concentrations over North China during North
476 China polluted days, about 90% of the total increase. In winter, eastern China is
477 dominated by strong northwesterly winds (Figure S6a). The anomalous southerly
478 winds during polluted days (relative to DJF average) over North China prevent the
479 high BC concentrations from being transported to South China, leading to a reduced
480 ventilation and accumulated aerosols in North China.

481 Over South China, BC concentrations increase by up to $2 \mu\text{g m}^{-3}$, in part due to
482 the transport from North China by anomalous northerly winds in the north part of
483 South China in South China polluted days. On average, contribution of North China
484 emissions to mean concentrations over South China increases by $1.2 \mu\text{g m}^{-3}$ (48% of
485 total increase) during the South China polluted days.

486 During polluted days in Southwest China, the anomalous northeasterly winds in
487 the east part of Southwest China bring in BC from the highly polluted eastern China,
488 resulting in $1.1 \mu\text{g m}^{-3}$ increase (53% of total increase) in the Southwest China, which
489 is as similar magnitude as the $1.0 \mu\text{g m}^{-3}$ contribution from the Southwest China local
490 emissions.

491 The increase in BC concentrations during polluted days over Central-West China
492 is also largely influenced by the accumulation effect of the anomalous winds over
493 eastern and central China, which also transport BC from Southwest and eastern
494 China into the receptor region.

495 The polluted days in Northeast China are caused by both the accumulation of
496 local emissions due to the reduced prevailing northeasterly winds and anomalous
497 transport of BC from North China.

498 Emissions from outside China could contribute to increases in BC concentrations
499 over Northwest China and Tibetan Plateau during polluted days. However, during
500 wintertime regional polluted days in eastern and central China, the contributions of
501 emissions from outside China do not have a significant influence on the changes in
502 BC concentrations.

503 These results suggest that the transport of aerosols plays an important role in
504 increasing BC concentrations during regional polluted days in eastern and central
505 China. Reductions in local emissions could benefit mitigation of both local and
506 non-local haze in China. Emissions from outside China are not as important to hazy
507 pollution in eastern and central China, where haze episodes occur frequently in winter
508 due to relatively high anthropogenic aerosol emissions and abnormal meteorological
509 conditions (Sun et al., 2014; R. H. Zhang et al., 2014; Yang et al., 2016). Note that, in
510 this study, we only focus on the source-receptor relationships related to the wind
511 anomalies during polluted days. In addition to winds, changes in other meteorological
512 fields, such as precipitation, temperature, humidity, and planetary boundary layer
513 height, could also influence the contributions of local aerosols between polluted and
514 normal days. Although the BC emissions used in the simulation include a seasonal
515 variability that could cause some variations in simulated concentrations, the monthly
516 variability in DJF of BC emissions is less than 4% over China, which is negligible
517 compared to the differences in concentrations between polluted and normal days.

518

519 **4.3. Source contributions to trans-boundary and trans-Pacific transport**

520 Considering the large contributions of emissions from South and Southeast Asia
521 to MAM BC concentrations in the southwest China (Figure 6) and the large outflow of
522 aerosols from East Asia in springtime (Yu et al., 2008), it is valuable to examine the
523 inflow and outflow of BC in China. Figures S8a and S8b show the vertical distribution
524 of source contributions of emissions from outside China to BC concentrations
525 averaged over 75°–120°E and 25°–35°N, respectively, around the south boundary of
526 continental China in MAM. High concentrations of BC originating from South and
527 Southeast Asia are lifted to the free atmosphere in the south slope of Tibetan Plateau.
528 Then westerly winds transport these BC particles to Southwest China and South
529 China in both low- and mid-troposphere. Figures S8c and S8d present the
530 contributions of emissions from China to BC concentrations averaged over 120°–
531 135°E and 20°–50°N, respectively, around the east boundary of continental China. In
532 MAM, the northward meridional winds over 25°–35°N and the southward meridional
533 winds over 40°–50°N lead to the accumulation of BC in the lower atmosphere in
534 eastern China. Westerly winds then transport these BC out of China mostly under
535 500 hPa.

536 Figure 10 shows the spatial distribution of column burden and surface
537 concentrations of BC resulting from emissions in and outside China in MAM. Column
538 burden is used to represent the outflow in this study following previous studies (Chin
539 et al., 2007; Hadley et al., 2007). There are strong outflows across the Pacific Ocean
540 originating from emissions both in and outside China. Emissions from China
541 contribute 0.19 mg m^{-2} (or 53%) of MAM mean BC along 150°E averaged over 20°–
542 60°N, whereas emissions outside China contribute 0.17 mg m^{-2} (or 47%). It suggests
543 that both emissions from China and outside China are important for the outflow from
544 East Asia. The yearly contribution from emissions from China to outflow from East
545 Asia in this study is 58%, similar to the contribution of 61% in Matsui et al. (2013)
546 calculated based on eastward BC mass flux using WRF-CMAQ model with INTEX-B
547 missions. Averaged over western United States (125°–105°W, 30°–50°N), emissions
548 from China account for 7% of near-surface BC concentrations and 25% in column
549 burden in MAM, indicating that emissions from China could have a significant impact

550 on air quality in western United States. More than half of the China contribution to BC
551 over western United States originates from eastern China (i.e., the tagged North and
552 South China).

553

554 **4.4. Source contributions to direct radiative forcing**

555 The high concentrations of BC in China could also have a significant impact on
556 the climate system through atmospheric heating or direct radiative forcing. As shown
557 in Figure 11, the annual mean direct radiative forcing (DRF) of BC at TOA is as high
558 as 3–4 $W m^{-2}$ at some locations. Similar to the source attributions of BC
559 concentrations (Figure 5) and burden (Figure S4), regional sources contribute the
560 largest to DRF over the respective local regions. Among all the source regions in
561 China, emissions from North, South, and Southwest China contribute the largest to
562 local DRF of BC, with maximum DRF in a range of 3–5, 2–3, and 3–5 $W m^{-2}$,
563 respectively. Other sources regions in China have relatively low contributions, with
564 maximum values less than 2 $W m^{-2}$. Emissions outside China lead to 1–2 $W m^{-2}$ of
565 DRF of BC over South, Southwest, Northwest China and Tibetan Plateau, and 0.2–1
566 $W m^{-2}$ over other parts of China, an effect that is quite widespread.

567 The total DRF of BC averaged over continental China simulated in this study is
568 2.27 $W m^{-2}$, larger than 0.64–1.55 $W m^{-2}$ in previous studies (Wu et al., 2008; Zhuang
569 et al., 2011; Li et al., 2016), probably due to the different emissions in the time periods
570 of study, as shown in Table S5. Emissions outside China have the largest
571 contributions to DRF of BC in China compared to any of the individual source regions
572 in China, with an averaged contribution of 0.77 $W m^{-2}$ (34%). This fractional
573 contribution from emissions outside China is larger than 25% in Li et al. (2016),
574 however we use different emissions, model and meteorology. Emissions from North
575 China result in 0.56 $W m^{-2}$ (25%) of DRF of BC over China, followed by 0.33 $W m^{-2}$
576 (15%) and 0.31 $W m^{-2}$ (14%) from South and Southwest China, respectively.
577 Emissions from Central-West, Northeast, Northwest China, and Tibetan Plateau
578 taken together account for 0.30 $W m^{-2}$ (13%) of DRF of BC over China.

579 Figure 12a shows the seasonal mean DRF of BC averaged over China as a
580 function of regional BC emissions. Because of high emissions, DRF of BC emitted
581 from North China is the largest in all seasons, with values in a range of 0.5–0.7 W m⁻²
582 averaged over China, followed by 0.2–0.5 W m⁻² from South and Southwest China.
583 BC from the other tagged regions in China contribute less than 0.2 W m⁻² in all
584 seasons. In general, BC DRF in each season is proportional to its emission rate.

585 Figure 12b presents the seasonal DRF efficiency of BC emitted from the tagged
586 regions and Table S6 summarizes these efficiencies. The variability of DRF efficiency
587 for forcing over China is determined by several factors, such as incoming solar
588 radiation (location of source regions), BC column burden and vertical distribution, and
589 transport out of the region. The China DRF efficiency is largest in western China (NW
590 and TP). This spatial pattern was also found by Henze et al. (2012). It can be
591 explained by the increase of multiple scattering effects and attenuation of the
592 transmitted radiation for large AOD (García et al., 2012). The Northeast China region
593 has a low China DRF efficiency due to transport eastward outside of China. The
594 remaining central and southern China regions have China DRF efficiencies that are
595 fairly consistent, varying by 20-30% about the average. The annual mean and
596 regional mean DRF efficiency in China is 0.91 W m⁻² Tg⁻¹, within the range of 0.41–
597 1.55 W m⁻² Tg⁻¹ from the previous studies (Table S5).

598 DRF efficiencies of BC from most regions have higher values in JJA and lower
599 values in DJF. This is primarily due to more incoming solar radiation in summer.
600 Insolation is the largest over Northwest China in JJA, together with less precipitation
601 than other regions, resulting in large DRF efficiency there. Global BC DRF efficiency,
602 particularly the annual average, is fairly similar for central, southern, and eastern
603 China regions (Fig. 12c, d). Global efficiency is still much higher for the western
604 regions.

605 BC emission reductions may impact mitigation of climate change and improve air
606 quality. To compare the relative importance of climate and air quality effects of BC
607 from different regions in China, Fig. 13 shows the near-surface concentration and
608 column burden efficiency of BC over China and globally and Table S7 summarizes

609 these efficiencies. For near-surface concentration (Fig. 13a and 13b), the efficiencies
610 are largest in DJF and lowest in JJA, in contrast to the DRF efficiencies, resulting
611 from the less precipitation and wet deposition of aerosols in winter. Unlike the DRF
612 efficiencies, the near-surface concentration efficiencies over eastern China are
613 similar and even larger than those for central and western China. These results
614 suggest that reduction in BC emissions in eastern China could benefit more on the
615 regional air quality in China, especially in winter haze season.

616 The relative distributions of column burden efficiencies (Fig. 13c and 13d) are
617 similar to the DRF efficiencies for the major emitting region in China, indicating that
618 aerosol lifetime in atmosphere drives DRF that influences regional and global climate.
619 The western regions (NW and TP), as expected, have a higher forcing per unit
620 column burden.

621

622 **5. Conclusions and discussions**

623 In this study, the Community Earth System Model (CESM) with a source-tagging
624 technique is used to quantify the contributions of BC emitted from seven regions in
625 continental China, including North China (NC), South China (SC), Southwest China
626 (SW), Central-West China (CW), Northeast China (NE), Northwest China (NW), and
627 Tibetan Plateau (TP), and sources outside China (RW) to concentrations, haze
628 formation, trans-boundary and trans-Pacific transport, and direct radiative forcing
629 (DRF) of BC in China. The anthropogenic emissions of BC for years 2010-2014 used
630 in this study were developed for the Coupled Model Intercomparison Project Phase 6
631 (CMIP6) from the Community Emissions Data System (CEDS). The annual total
632 emission of BC from continental China is 2497 Gg C averaged over years 2010–2014.
633 The model captures well the spatial distribution and seasonal variation in China.
634 AAOD compares well with measurements, which are largely located in central and
635 eastern China. Surface BC concentrations are underestimated by 53% compared to
636 point observations.

637 The individual source regions are the largest contributors to their local BC
638 concentration levels. Over North China where the air quality is often poor, about 90%

639 of near-surface BC concentration is contributed by local emissions. However, some
640 source regions also impact BC in neighboring regions. Due to the seasonal variability
641 of winds and emission rates, emissions from North China account for 30% of
642 near-surface BC concentrations over South China in DJF
643 (December-January-February), while emissions from outside China contribute about
644 10% in MAM (March-April-May). Over Southwest China, 17% of BC in MAM comes
645 from sources outside China. Southwest and North China emissions contribute largely
646 to BC in Central-West China. North China emissions have a contribution in a range of
647 12–36% to BC concentrations in Northeast China. Over Northwest China and Tibetan
648 Plateau, more than 20% and 40% of BC, respectively, originates from emissions
649 outside China. These indicate that, for regions with high emissions, their BC
650 concentrations are dominated by local emissions. In contrast, BC levels over central
651 and western China with lower emissions are more strongly influenced by non-local
652 emissions. For all continental China as a whole, seasonal BC concentrations are
653 largely due to emissions from North and South China, with relative contributions
654 ranging from 43–50% and 18–24%, respectively, followed by contributions from
655 Southwest (10–13%) and outside China (4–12%).

656 Emissions from non-local sources together with abnormal winds are one of the
657 important factors contributing to high winter time pollution events in China. Over
658 South China, about 50% of the increase in BC concentrations during high pollution
659 conditions results from North China emissions. The increases in BC concentrations
660 during polluted days over Southwest, Central-West and Northeast China are strongly
661 influenced by emissions from eastern China. Emissions from outside China could
662 contribute significantly to increases in BC concentrations over Northwest China and
663 Tibetan Plateau during their polluted days. However, emissions from outside China
664 do not have a significant contribution to haze in eastern and central China,
665 suggesting that reduction in emissions within China would be needed to mitigate both
666 local and non-local BC concentrations under high-polluted conditions.

667 Emissions from regions in and outside China both account for about half of BC
668 outflow from East Asia, suggesting that emissions from China and other regions are

669 equally important for the BC outflow from East Asia. Through long-range transport,
670 emissions from China result in 7% of near-surface BC concentration and 25% in
671 column burden over western United States in MAM, indicating that emissions from
672 China could have an impact on air quality in western United States.

673 The total DRF of BC averaged over continental China simulated in this study is
674 2.27 W m^{-2} . Among the tagged regions, emissions outside China have the largest
675 single contribution to DRF of BC in China, with an average contribution of 34%,
676 followed by 25%, 15%, and 14% due to emissions from North, South and Southwest
677 China, respectively. DRF efficiencies over eastern China are small compared to
678 central and western China in all seasons. For near-surface concentration, the
679 efficiencies are largest in DJF and lowest in JJA, and efficiencies over eastern China
680 are similar and even larger than central and western China. These suggest that
681 reduction in BC emissions over eastern China could benefit more on the regional air
682 quality in China, especially in winter haze season.

683 Note that the model largely underestimates BC concentrations over China,
684 compared to the observation, which has also been reported in many previous studies
685 using different models and different emission inventories (e.g., Liu et al., 2012; Fu et
686 al., 2012; Huang et al., 2013; H. Wang et al., 2013; Q. Wang et al., 2014; R. Wang et
687 al., 2014; Li et al., 2016). One possible reason is that in situ measurements are point
688 observations, while the model does not treat the subgrid variability of aerosols and
689 assumes aerosols are uniformly distributed over the grid cell. R. Wang et al. (2014)
690 found a reduction of negative bias (from -88% to -35%) in the modeled surface BC
691 concentrations when using high-resolution emissions and modeling at $0.5^\circ \times 0.7^\circ$
692 resolution. This result indicates that the siting of observational stations can result in
693 an artificial bias when comparing with relatively coarse model results. Further
694 investigation of this siting/resolution bias is warranted, including investigation on
695 whether this type of bias might extend, presumably to a lesser extent, also to AAOD
696 measurements.

697 Further reasons that could contribute to this bias are emission underestimation or
698 inaccurate aerosol processes in the model. Given that the differences between

699 modeled and observed AAOD over eastern China are relatively small (−18%), we
700 conclude that, given current evidence, the total amount of atmospheric BC in these
701 simulations is reasonable at least in this sub-region.

702 Over eastern China, the BC concentrations are dominated by local emissions in
703 this study, with local contribution of 64–93%. The underestimation of simulated BC
704 concentrations over eastern China is more likely due to either underestimation of
705 local emissions, too much aerosol removal within these regions, or resolution bias
706 between observations and model grids. Over western China, 22–76% of the BC
707 originates from emissions outside China. Thus biases of simulated BC concentrations
708 could also come from underestimation of emissions outside China and or too much
709 removal of BC during long-range transport. Satellite data are a promising method to
710 validate modeling and emissions inventories, given that they do not depend on the
711 location of observing stations, providing more uniform spatial coverage. A
712 comparison of modeled AAOD and satellite AI provides an indication that the
713 modeled burden in western China is underestimated, although the role of dust needs
714 to be better characterized.

715 Uncertainty in China BC emissions has been estimated as −43% to 93% by Lu et
716 al. (2011), −50% to 164% by Qin and Xie (2012), ±176% by Kurokawa et al. (2013),
717 and −28 to 126% by Zhao et al. (2013). The BC emissions estimates used here for
718 China in 2010 are 40% higher than those of Zhao et al. (2013) and Lu et al. (2011)
719 and 30% higher than Klimont et al. (2016), in large part due to a higher estimate of
720 BC emissions from coal coke production. Emissions from coke production are
721 particularly uncertain given that “there are no measurements for PM_{2.5} and BC
722 emissions” (Huo et al. 2012) available to guide inventory estimates. Total rest of the
723 world emissions other than China, which appear to be a major contributor to burdens
724 over western regions, are within 1% of those from Klimont et al. (2016).

725 BC aging in the atmosphere is important for BC concentration and its optical
726 properties, which transforms BC from hydrophobic aggregates to hydrophilic particles
727 coated with soluble materials. He et al. (2015, 2016a) found that BC optical properties
728 varied by a factor of two or more due to different coating structures during BC aging

729 process based on their theoretical and experimental intercomparison. Oshima et al.
730 (2009) and He et al. (2016b) pointed out that the use of various microphysical BC
731 aging schemes could significantly improve simulations of BC concentrations,
732 compared to the simplified aging parameterizations. Liu et al. (2012) also reported
733 that the wet removal rate of BC simulated in standard CAM5 is 60% higher than
734 AeroCom multi-model mean due to the rapid or instantaneous aging of BC. H. Wang
735 et al. (2013) showed that the explicit treatment of BC aging process with slow aging
736 assumptions in CAM5 could significantly increase BC lifetime and the efficiency of BC
737 long-range transport. In the three-mode aerosol module (MAM3) of CAM5 used in this
738 study, the aging process of BC is neglected by assuming the immediate internal
739 mixing of BC with other aerosol species in the same mode. This assumption could
740 lead to an overestimation of wet removal of BC and, therefore, an underestimation of
741 BC concentrations, absorption optical depth (Fig. 3) and direct radiative forcing. In
742 addition, the internally-mixed optical treatment in CAM5 could also cause bias in BC
743 absorption calculation. However, H. Wang et al. (2014) examined source-receptor
744 relationships for BC under the different BC aging assumptions and found that the
745 quantitative source attributions varied slightly while the qualitative source-receptor
746 relationships still hold. Therefore, although the magnitude of simulated BC and its
747 optical properties could be underestimated due to the instantaneous aging of BC and
748 uncertainty in coating structures, we expect that the aging treatment in MAM3 of
749 CAM5 should not influence the qualitative source attributions examined in this study.

750 In this study, BC is used as an indicator of pollution (or air quality) in China.
751 Although BC is often co-emitted with other species, such as primary organic matter,
752 organic gases and sulfuric gases, source-receptor relationship of BC may not fully
753 represent that of total aerosols. The contribution of BC to total near-surface PM_{2.5}
754 concentrations averaged over China is less than 10%. Other aerosols, such as
755 sulfate, are dominant in China during polluted days. The spatio-temporal variations
756 and source contributions of these species are largely different from those of BC
757 because spatial distributions of emissions (e.g., SO₂) and formation processes can
758 be considerably different. For example, Matsui et al. (2009) showed that primary

759 aerosols around Beijing were determined by emissions within 100 km around Beijing
760 within the preceding 24 hours, while emissions as far as 500 km and within the
761 preceding 3 days were found to affect secondary aerosols in Beijing. Thus, the
762 secondary aerosols could have larger contributions from non-local emissions than BC.
763 BC concentrations are highest in winter over China due to higher emissions, while
764 sulfate concentrations reach maximum in summer when the strong sunlight and high
765 temperature favor the sulfate formation. Therefore, knowing the accurate source
766 attributions of air pollution in China requires source tagging for more aerosol species,
767 such as sulfate.

768

769 *Acknowledgments.*

770 This research was supported by the National Atmospheric and Space
771 Administration's Atmospheric Composition: Modeling and Analysis Program
772 (ACMAP), award NNH15AZ64I. We also acknowledge additional support from the
773 U.S. Department of Energy (DOE), Office of Science, Biological and
774 Environmental Research. The Pacific Northwest National Laboratory is
775 operated for DOE by Battelle Memorial Institute under contract
776 DE-AC05-76RLO1830. The CESM project was supported by the National Science
777 Foundation and the DOE Office of Science. The satellite-derived Total Ozone
778 Mapping Spectrometer Aerosol Index monthly data sets are obtained from the Web
779 site at http://disc.sci.gsfc.nasa.gov/data-holdings/PIP/aerosol_index.shtml. The
780 National Energy Research Scientific Computing Center (NERSC) provided
781 computational resources. Model results are available through NERSC upon request.

782 **References**

783

784 Abdul-Razzak, H., and Ghan, S. J.: A parameterization of aerosol activation: 2.

785 Multiple aerosol types, *J. Geophys. Res.*, 105, 6837–6844,

786 doi:10.1029/1999JD901161, 2000.

787

788 Anenberg, S. C., Talgo, K., Arunachalam, S., Dolwick, P., Jang, C., and West, J. J.:

789 Impacts of global, regional, and sectoral black carbon emission reductions on

790 surface air quality and human mortality, *Atmos. Chem. Phys.*, 11, 7253-7267,

791 doi:10.5194/acp-11-7253-2011, 2011.

792

793 Bond, T. C., Streets, D. G., Yarber, K. F., Nelson, S. M., Woo, J.-H., and Klimont, Z.:

794 A technology-based global inventory of black and organic carbon emissions from

795 combustion, *J. Geophys. Res.*, 109, D14203, doi:10.1029/2003JD003697, 2004.

796

797 Bond, T. C., and Bergstrom, R. W.: Light absorption by carbonaceous particles: An

798 investigative review, *Aerosol. Sci. Technol.*, 40, 27–67,

799 doi:10.1080/02786820500421521, 2006.

800

801 Bond, T. C., Bhardwaj, E., Dong, R., Jogani, R., Jung, S., Roden, C., Streets, D. G.,

802 and Trautmann, N. M.: Historical emissions of black and organic carbon aerosol

803 from energy-related combustion, 1850–2000, *Global Biogeochem. Cycles*, 21,

804 GB2018, doi:10.1029/2006GB002840, 2007.

805

806 Bond, T. C., Doherty, S. J., Fahey, D. W., Forster, P. M., Berntsen, T., DeAngelo, B.
807 J., Flanner, M. G., Ghan, S., Kärcher, B., Koch, D., Kinne, S., Kondo, Y., Quinn,
808 P. K., Sarofim, M. C., Schultz, M. G., Schulz, M., Venkataraman, C., Zhang, H.,
809 Zhang, S., Bellouin, N., Guttikunda, S. K., Hopke, P. K., Jacobson, M. Z.,
810 Kaiser, J. W., Klimont, Z., Lohmann, U., Schwarz, J. P., Shindell, D., Storelvmo,
811 T., Warren, S. G., and Zender, C. S.: Bounding the role of black carbon in the
812 climate system: A scientific assessment, *J. Geophys. Res.*, 118, 5380–5552,
813 doi:10.1002/jgrd.50171, 2013.

814

815 Chin, M., Diehl, T., Ginoux, P., and Malm, W.: Intercontinental transport of pollution
816 and dust aerosols: implications for regional air quality, *Atmos. Chem. Phys.*, 7,
817 5501-5517, doi:10.5194/acp-7-5501-2007, 2007.

818

819 Ding, Y. H., and Liu, Y. J.: Analysis of long-term variations of fog and haze in China in
820 recent 50 years and their relations with atmospheric humidity, *Sci. China Earth*
821 *Sci.*, 57, 36–46, doi:10.1007/s11430-013-4792-1, 2014.

822

823 Flanner, M. G., Zender, C. S., Randerson, J. T., and Rasch, P. J.: Present day
824 climate forcing and response from black carbon in snow, *J. Geophys. Res.*, 112,
825 D11202, doi:10.1029/2006JD008003, 2007.

826

827 Fu, T.-M., Cao, J. J., Zhang, X. Y., Lee, S. C., Zhang, Q., Han, Y. M., Qu, W. J., Han,
828 Z., Zhang, R., Wang, Y. X., Chen, D., and Henze, D. K.: Carbonaceous aerosols
829 in China: top-down constraints on primary sources and estimation of secondary
830 contribution, *Atmos. Chem. Phys.*, 12, 2725-2746,
831 doi:10.5194/acp-12-2725-2012, 2012.

832

833 García, O. E., Díaz, J. P., Expósito, F. J., Díaz, A. M., Dubovik, O., Derimian, Y.,
834 Dubuisson, P., and Roger, J.-C.: Shortwave radiative forcing and efficiency of key
835 aerosol types using AERONET data, *Atmos. Chem. Phys.*, 12, 5129-5145,
836 doi:10.5194/acp-12-5129-2012, 2012.

837

838 Ghan, S. J., and Zaveri, R. A.: Parameterization of optical properties for hydrated
839 internally mixed aerosol, *J. Geophys. Res.*, 112, D10201,
840 doi:10.1029/2006JD007927, 2007.

841

842 Ghan, S. J., Technical Note: Estimating aerosol effects on cloud radiative forcing,
843 *Atmos. Chem. Phys.*, 13, 9971-9974, doi:10.5194/acp-13-9971-2013, 2013.

844

845 Hadley, O. L., Ramanathan, V., Carmichael, G. R., Tang, Y., Corrigan, C. E.,
846 Roberts, G. C., and Mauger, G. S.: Trans-Pacific transport of black carbon and
847 fine aerosols ($D < 2.5 \mu\text{m}$) into North America, *J. Geophys. Res.*, 112, D05309,
848 doi:10.1029/2006JD007632, 2007.

849

850 He, C., Liou, K.-N., Takano, Y., Zhang, R., Levy Zamora, M., Yang, P., Li, Q., and
851 Leung, L. R.: Variation of the radiative properties during black carbon aging:
852 theoretical and experimental intercomparison, *Atmos. Chem. Phys.*, 15,
853 11967-11980, doi:10.5194/acp-15-11967-2015, 2015.

854

855 He, C., Takano, Y., Liou, K.-N., Yang, P., Li, Q., and Mackowski, D. W.:
856 Intercomparison of the GOS approach, superposition T- matrix method, and
857 laboratory measurements for black carbon optical properties during aging, *J.*
858 *Quant. Spectrosc. Ra.*, 184, 287–296, doi:10.1016/j.jqsrt.2016.08.004, 2016a.

859

860 He, C., Li, Q., Liou, K.-N., Qi, L., Tao, S., and Schwarz, J. P.: Microphysics-based
861 black carbon aging in a global CTM: constraints from HIPPO observations and
862 implications for global black carbon budget, *Atmos. Chem. Phys.*, 16, 3077-3098,
863 doi:10.5194/acp-16-3077-2016, 2016b.

864

865 Henze, D. K., Shindell, D. T., Akhtar, F., R. Spurr, J. D., Pinder, R. W., Loughlin, D.,
866 Kopacz, M., Singh, K., and Shim, C.: Spatially refined aerosol direct radiative
867 forcing efficiencies, *Environ. Sci. Technol.*, 46, 9511–9518,
868 doi:10.1021/es301993s, 2012.

869

870 Holben, B. N., Tanré, D., Smirnov, A., Eck, T. F., Slutsker, I., Abuhassan, N.,
871 Newcomb, W. W., Schafer, J. S., Chatenet, B., Lavenu, F., Kaufman, Y. J.,
872 Castle, J. V., Setzer, A., Markham, B., Frouin, D. C. R., Halthore, R., Karneli, A.,
873 O'Neill, N. T., Pietras, C., Pinker, R. T., Voss, K., and Zibordi, G.: An emerging
874 ground-based aerosol climatology: Aerosol optical depth from AERONET, *J.*
875 *Geophys. Res.*, 106, 12 067–12 098, 2001.

876

877 Huang, Y., Wu, S., Dubey, M. K., and French, N. H. F.: Impact of aging mechanism
878 on model simulated carbonaceous aerosols, *Atmos. Chem. Phys.*, 13,
879 6329-6343, doi:10.5194/acp-13-6329-2013, 2013.

880

881 Huo, H., Lei, Y., Zhang, Q., Zhao, L. J., and He, K. B.: China's coke industry: Recent
882 policies, technology shift, and implication for energy and the environment, *Energ.*
883 *Policy.*, 51, 397–404, doi:10.1016/j.enpol.2012.08.041, 2012.

884

885 Hurrell, J. W., Holland, M. M., Gent, P. R., Ghan, S., Kay, J. E., Kushner, P. J.,
886 Lamarque, J. F., Large, W. G., Lawrence, D., Lindsay, K., Lipscomb, W. H.,
887 Long, M. C., Mahowald, N., Marsh, D. R., Neale, R. B., Rasch, P., Vavrus, S.,
888 Vertenstein, M., Bader, D., Collins, W. D., Hack, J. J., Kiehl, J., and Marshall, S.:
889 The Community Earth System Model A Framework for Collaborative Research,
890 *B. Am. Meteorol. Soc.*, 94, 1339–1360, 2013.

891

892 IPCC, 2013, Climate Change 2013: the Physical Science Basis. Contribution of
893 Working Group I to the Fifth Assessment Report of the Intergovernmental Panel
894 on Climate Change. Cambridge University Press, Cambridge, United Kingdom
895 and New York, NY, USA, p. 1535.

896

897 Jacobson, M. Z.: Effects of externally-through-internally-mixed soot inclusions within
898 clouds and precipitation on global climate, *J. Phys. Chem. A*, 110, 6860–6873,
899 doi:10.1021/Jp056391r, 2006.

900

901 Janssen, N. A. H., Gerlofs-Nijiland, M. E., Lanki, T., Salonen, R. O., Cassee, F.,
902 Hoek, G., Fischer, P., Brunekreef, B., and Krzyzanowski, M.: Health Effects of
903 Black Carbon, World Health Organization, Copenhagen, 2012.

904

905 Janssens-Maenhout, G., Crippa, M., Guizzardi, D., Dentener, F., Muntean, M.,
906 Pouliot, G., Keating, T., Zhang, Q., Kurokawa, J., Wankmüller, R., Denier van der
907 Gon, H., Kuenen, J. J. P., Klimont, Z., Frost, G., Darras, S., Koffi, B., and Li, M.:
908 HTAP_v2.2: a mosaic of regional and global emission grid maps for 2008 and
909 2010 to study hemispheric transport of air pollution, *Atmos. Chem. Phys.*, 15,
910 11411-11432, doi:10.5194/acp-15-11411-2015, 2015.

911

912 Jiao, C., Flanner, M. G., Balkanski, Y., Bauer, S. E., Bellouin, N., Berntsen, T. K.,
913 Bian, H., Carslaw, K. S., Chin, M., De Luca, N., Diehl, T., Ghan, S. J., Iversen, T.,

914 Kirkevåg, A., Koch, D., Liu, X., Mann, G. W., Penner, J. E., Pitari, G., Schulz, M.,
915 Seland, Ø., Skeie, R. B., Steenrod, S. D., Stier, P., Takemura, T., Tsigaridis, K.,
916 van Noije, T., Yun, Y., and Zhang, K.: An AeroCom assessment of black carbon
917 in Arctic snow and sea ice, *Atmos. Chem. Phys.*, 14, 2399-2417,
918 doi:10.5194/acp-14-2399-2014, 2014.

919

920 Klimont, Z., Kupiainen, K., Heyes, C., Purohit, P., Cofala, J., Rafaj, P.,
921 Borken-Kleefeld, J., and Schöpp, W.: Global anthropogenic emissions of
922 particulate matter including black carbon, *Atmos. Chem. Phys. Discuss.*,
923 doi:10.5194/acp-2016-880, in review, 2016.

924

925 Koepke, M. H. P., and Schult, I.: Optical properties of aerosols and clouds: The
926 software package opac, *Bull. Am. Meteorol. Soc.*, 79, 831–844,
927 doi:10.1175/1520-0477(1998)079<0831:OPOAAC>2.0.CO;2, 1998.

928

929 Kristiansen, N. I., Stohl, A., Olivié, D. J. L., Croft, B., Søvde, O. A., Klein, H.,
930 Christoudias, T., Kunkel, D., Leadbetter, S. J., Lee, Y. H., Zhang, K., Tsigaridis,
931 K., Bergman, T., Evangeliou, N., Wang, H., Ma, P.-L., Easter, R. C., Rasch, P. J.,
932 Liu, X., Pitari, G., Di Genova, G., Zhao, S. Y., Balkanski, Y., Bauer, S. E.,
933 Faluvegi, G. S., Kokkola, H., Martin, R. V., Pierce, J. R., Schulz, M., Shindell, D.,
934 Tost, H., and Zhang, H.: Evaluation of observed and modelled aerosol lifetimes

935 using radioactive tracers of opportunity and an ensemble of 19 global models,
936 *Atmos. Chem. Phys.*, 16, 3525-3561, doi:10.5194/acp-16-3525-2016, 2016.

937

938 Kurokawa, J., Ohara, T., Morikawa, T., Hanayama, S., Janssens-Maenhout, G.,
939 Fukui, T., Kawashima, K., and Akimoto, H.: Emissions of air pollutants and
940 greenhouse gases over Asian regions during 2000–2008: Regional Emission
941 inventory in ASia (REAS) version 2, *Atmos. Chem. Phys.*, 13, 11019-11058,
942 doi:10.5194/acp-13-11019-2013, 2013.

943

944 Lau, K.-M., Kim, M. K., Kim, K.-M., and Lee, W. S.: Enhanced surface warming and
945 accelerated snow melt in the Himalayas and Tibetan Plateau induced by
946 absorbing aerosols, *Environ. Res. Lett.*, 5, 025204,
947 doi:10.1088/1748-9326/5/2/025204, 2010.

948

949 Li, K., Liao, H., Mao, Y. H., and Ridley, D. A.: Source sector and region contributions
950 to concentration and direct radiative forcing of black carbon in China, *Atmos.*
951 *Environ.*, 124, 351–366, doi:10.1016/j.atmosenv.2015.06.014, 2016.

952

953 Liao, H., Chang, W. Y., and Yang, Y.: Climatic effects of air pollutants over China: A
954 review, *Adv. Atmos. Sci.*, 32, 115–139, doi:10.1007/s00376-014-0013-x, 2015.

955

956 Liu, X., Easter, R. C., Ghan, S. J., Zaveri, R., Rasch, P., Shi, X., Lamarque, J.-F.,
957 Gettelman, A., Morrison, H., Vitt, F., Conley, A., Park, S., Neale, R., Hannay, C.,
958 Ekman, A. M. L., Hess, P., Mahowald, N., Collins, W., Iacono, M. J., Bretherton,
959 C. S., Flanner, M. G., and Mitchell, D.: Toward a minimal representation of
960 aerosols in climate models: description and evaluation in the Community
961 Atmosphere Model CAM5, *Geosci. Model Dev.*, 5, 709-739,
962 doi:10.5194/gmd-5-709-2012, 2012.

963

964 Liu, X., Ma, P.-L., Wang, H., Tilmes, S., Singh, B., Easter, R. C., Ghan, S. J., and
965 Rasch, P. J.: Description and evaluation of a new four-mode version of the Modal
966 Aerosol Module (MAM4) within version 5.3 of the Community Atmosphere Model,
967 *Geosci. Model Dev.*, 9, 505-522, doi:10.5194/gmd-9-505-2016, 2016.

968

969 Lou, S., Russell, L. M., Yang, Y., Xu, L., Lamjiri, M. A., DeFlorio, M. J., Miller, A. J.,
970 Ghan, S. J., Liu, Y., and Singh, B.: Impacts of the East Asian Monsoon on
971 springtime dust concentrations over China, *J. Geophys. Res. Atmos.*, 121, 8137–
972 8152, doi:10.1002/2016JD024758, 2016.

973

974 Lu, Z., Zhang, Q., and Streets, D. G.: Sulfur dioxide and primary carbonaceous
975 aerosol emissions in China and India, 1996–2010, *Atmos. Chem. Phys.*, 11,
976 9839-9864, doi:10.5194/acp-11-9839-2011, 2011.

977

978 Ma, P.-L., Gattiker, J. R., Liu, X., and Rasch, P. J.: A novel approach for determining
979 source-receptor relationships in model simulations: a case study of black carbon
980 transport in northern hemisphere winter, *Environ. Res. Lett.*, 8(2), 024042,
981 doi:10.1088/1748-9326/8/2/024042, 2013a.

982

983 Ma, P.-L., Rasch, P. J., Wang, H., Zhang, K., Easter, R. C., Tilmes, S., Fast, J. D.,
984 Liu, X., Yoon, J.-H., and Lamarque, J.-F.: The role of circulation features on black
985 carbon transport into the Arctic in the Community Atmosphere Model version 5
986 (CAM5), *J. Geophys. Res. Atmos.*, 118, 4657–4669, doi:10.1002/jgrd.50411,
987 2013b.

988

989 Matsui, H., Koike, M., Kondo, Y., Takegawa, N., Kita, K., Miyazaki, Y., Hu, M., Chang,
990 S.-Y., Blake, D. R., Fast, J. D., Zaveri, R. A., Streets, D. G., Zhang, Q., and Zhu,
991 T.: Spatial and temporal variations of aerosols around Beijing in summer 2006:
992 Model evaluation and source apportionment, *J. Geophys. Res.*, 114, D00G13,
993 doi:10.1029/2008JD010906, 2009.

994

995 Matsui, H., Koike, M., Kondo, Y., Oshima, N., Moteki, N., Kanaya, Y., Takami, A., and
996 Irwin, M.: Seasonal variations of Asian black carbon outflow to the Pacific:
997 Contribution from anthropogenic sources in China and biomass burning sources
998 in Siberia and Southeast Asia, *J. Geophys. Res. Atmos.*, 118, 9948–9967,
999 doi:10.1002/jgrd.50702, 2013.

1000

1001 McFarquhar, G., and Wang, H.: Effects of aerosols on trade wind cumuli over the
1002 Indian Ocean: Model simulations, *Q. J. R. Meteorol. Soc.*, 132, 821–843,
1003 doi:10.1256/qj.04.179, 2006.

1004

1005 Oshima, N., Koike, M., Zhang, Y., Kondo, Y., Moteki, N., Takegawa, N., and
1006 Miyazaki, Y.: Aging of black carbon in outflow from anthropogenic sources using
1007 a mixing state resolved model: Model development and evaluation, *J. Geophys.
1008 Res.*, 114, D06210, doi:10.1029/2008JD010680, 2009.

1009

1010 Oshima, N., Kondo, Y., Moteki, N., Takegawa, N., Koike, M., Kita, K., Matsui, H.,
1011 Kajino, M., Nakamura, H., Jung, J. S., and Kim, Y. J.: Wet removal of black
1012 carbon in Asian outflow: Aerosol Radiative Forcing in East Asia (A-FORCE)
1013 aircraft campaign, *J. Geophys. Res.*, 117, D03204, doi:10.1029/2011jd016552,
1014 2012.

1015

1016 Qian, Y., Flanner, M. G., Leung, L. R., and Wang, W.: Sensitivity studies on the
1017 impacts of Tibetan Plateau snowpack pollution on the Asian hydrological cycle
1018 and monsoon climate, *Atmos. Chem. Phys.*, 11, 1929-1948,
1019 doi:10.5194/acp-11-1929-2011, 2011.

1020

1021 Qian, Y., Wang, H., Zhang, R., Flanner, M. G., and Rasch, P. J.: A sensitivity study on
1022 modeling black carbon in snow and its radiative forcing over the Arctic and
1023 Northern China, *Environ. Res. Lett.*, 9, 064001,
1024 doi:10.1088/1748-9326/9/6/064001, 2014.

1025

1026 Qian, Y., Yasunari, T. J., Doherty, S. J., Flanner, M. G., Lau, W. K. M., Ming, J.,
1027 Wang, H., Wang, M., Warren, S. G., and Zhang, R.: Light-absorbing particles in
1028 snow and ice: Measurement and modeling of climatic and hydrological impact,
1029 *Adv. Atmos. Sci.*, 32(1), 64–91, doi:10.1007/s00376-014-0010-0, 2015.

1030

1031 Qin, Y. and Xie, S. D.: Spatial and temporal variation of anthropogenic black carbon
1032 emissions in China for the period 1980–2009, *Atmos. Chem. Phys.*, 12,
1033 4825–4841, doi:10.5194/acp-12-4825-2012, 2012.

1034

1035 Ramanathan, V., and Carmichael, G.: Global and regional climate changes due to
1036 black carbon, *Nat. Geosci.*, 1, 221–227, doi:10.1038/ngeo156, 2008.

1037

1038 Rienecker, M. M., Suarez, M. J., Gelaro, R., Todling, R., Bacmeister, J., Liu, R.,
1039 Bosilovich, M. G., Schubert, S. D., Takacs, L., Kim, G-K, Bloom, S., Chen, J.,
1040 Collins, D., Conaty, A., da Silva, A., Gu, W., Joiner, J., Koster, R. D., Lucchesi,
1041 R., Molod, A., Owens, T., Pawson, S., Pegion, P., Redder, C. R., Reichle, R.,
1042 Robertson, F. R., Ruddick, A. G., Sienkiewicz, M., and Woollen, J.: MERRA:

1043 NASA's Modern-Era Retrospective Analysis for Research and Applications, J.
1044 Climate, 24, 3624–3648, 2011.

1045

1046 Schuster, G. L., Dubovik, O., Arola, A., Eck, T. F., and Holben, B. N.: Remote sensing
1047 of soot carbon – Part 2: Understanding the absorption Ångström exponent,
1048 Atmos. Chem. Phys., 16, 1587-1602, doi:10.5194/acp-16-1587-2016, 2016.

1049

1050 Shindell, D., et al. (2012), Simultaneously mitigating near-term climate change and
1051 improving human health and food security, Science, 335(6065), 183-189,
1052 doi:10.1126/science.1210026.

1053

1054 Shindell, D., Kuylenstierna, J. C. I., Vignati, E., van Dingenen, R., Amann, M.,
1055 Klimont, Z., Anenberg, S. C., Muller, N., Janssens- Maenhout, G., Raes, F.,
1056 Schwartz, J., Faluvegi, G., Pozzoli, L., Kupiainen, K., Höglund-Isaksson, L.,
1057 Emberson, L., Streets, D., Ramanathan, V., Hicks, K., Oanh, N. T. K., Milly, G.,
1058 Williams, M., Demkine, V., and Fowler, D.: Simultaneously Mitigating Near-Term
1059 Climate Change and Improving Human Health and Food Security, Science, 335,
1060 183–189, doi:10.1126/science.1210026, 2012.

1061

1062 Smith, S. J., and Mizrahi, A.: Near-term climate mitigation by short-lived forcings, Proc.
1063 Natl. Acad. Sci, 110(35), 14202-14206, doi:10.1073/pnas.1308470110, 2013.

1064

1065 Sun, Y., Jiang, Q., Wang, Z., Fu, P., Li, J., Yang, T., and Yin, Y.: Investigation of the
1066 sources and evolution processes of severe haze pollution in Beijing in January
1067 2013, *J. Geophys. Res. Atmos.*, 119, 4380–4398, doi:10.1002/2014JD021641,
1068 2014.

1069

1070 Wang, H., Easter, R. C., Rasch, P. J., Wang, M., Liu, X., Ghan, S. J., Qian, Y., Yoon,
1071 J.-H., Ma, P.-L., and Vinoj, V.: Sensitivity of remote aerosol distributions to
1072 representation of cloud–aerosol interactions in a global climate model, *Geosci.*
1073 *Model Dev.*, 6, 765-782, doi:10.5194/gmd-6-765-2013, 2013.

1074

1075 Wang, H., Rasch, P. J., Easter, R. C., Singh, B., Zhang, R., Ma, P.-L., Qian, Y., Ghan,
1076 S. J., and Beagley, N.: Using an explicit emission tagging method in global
1077 modeling of source-receptor relationships for black carbon in the Arctic:
1078 Variations, sources, and transport pathways, *J. Geophys. Res. Atmos.*, 119,
1079 12,888–12,909, doi:10.1002/2014JD022297, 2014.

1080

1081 Wang, L. T., Wei, Z., Yang, J., Zhang, Y., Zhang, F. F., Su, J., Meng, C. C., and
1082 Zhang, Q.: The 2013 severe haze over southern Hebei, China: model evaluation,
1083 source apportionment, and policy implications, *Atmos. Chem. Phys.*, 14,
1084 3151-3173, doi:10.5194/acp-14-3151-2014, 2014.

1085

1086 Wang, M., Ghan, S., Ovchinnikov, M., Liu, X., Easter, R., Kassianov, E., Qian, Y., and
1087 Morrison, H.: Aerosol indirect effects in a multi-scale aerosol-climate model
1088 PNNL-MMF, *Atmos. Chem. Phys.*, 11, 5431-5455,
1089 doi:10.5194/acp-11-5431-2011, 2011.

1090

1091 Wang, Q., Jacob, D. J., Spackman, J. R., Perring, A. E., Schwarz, J. P., Moteki, N.,
1092 Marais, E. A., Ge, C., Wang, J., and Barrett, S. R. H.: Global budget and
1093 radiative forcing of black carbon aerosol: Constraints from pole-to-pole (HIPPO)
1094 observations across the Pacific, *J. Geophys. Res.-Atmos.*, 119, 195–206,
1095 doi:10.1002/2013jd020824, 2014.

1096

1097 Wang, R., Tao, S., Balkanski, Y., Ciais, P., Boucher, O., Liu, J., Piao, S., Shen, H.,
1098 Vuolo, M. R., and Valari, M.: Exposure to ambient black carbon derived from a
1099 unique inventory and high-resolution model, *P. Natl. Acad. Sci. USA*, 111, 2459–
1100 2463, 2014.

1101

1102 Wang, X., Wang, Y., Hao, J., Kondo, Y., Irwin, M., Munger, J. W., and Zhao, Y.:
1103 Top-down estimate of China's black carbon emissions using surface
1104 observations: Sensitivity to observation representativeness and transport model
1105 error, *J. Geophys. Res. Atmos.*, 118, 5781–5795, doi:10.1002/jgrd.50397, 2013.

1106

1107 Wu, J., Fu, C., Xu, Y., Tang, J. P., Wang, W., and Wang, Z.: Simulation of direct
1108 effects of black carbon aerosol on temperature and hydrological cycle in Asia by a
1109 Regional Climate Model, *Meteorol. Atmos. Phys.*, 100(1), 179–193,
1110 doi:10.1007/s00703-008-0302-y, 2008.

1111

1112 Yang, Y., Liao, H., and Lou, S.: Decadal trend and interannual variation of outflow of
1113 aerosols from East Asia: Roles of variations in meteorological parameters and
1114 emissions, *Atmos. Environ.*, 100, 141-153, doi:10.1016/j.atmosenv.2014.11.004,
1115 2015.

1116

1117 Yang, Y., Liao, H., and Lou, S.: Increase in winter haze over eastern China in recent
1118 decades: Roles of variations in meteorological parameters and anthropogenic
1119 emissions, *J. Geophys. Res. Atmos.*, 121, doi:10.1002/2016JD025136, 2016.

1120

1121 Yu, H., Remer, L. A., Chin, M., Bian, H., Kleidman, R. G., and Diehl, T.: A
1122 satellite-based assessment of transpacific transport of pollution aerosol, *J.*
1123 *Geophys. Res.*, 113, D14S12, doi:10.1029/2007JD009349, 2008.

1124

1125 Zhang, K., Wan, H., Liu, X., Ghan, S. J., Kooperman, G. J., Ma, P.-L., Rasch, P. J.,
1126 Neubauer, D., and Lohmann, U.: Technical Note: On the use of nudging for
1127 aerosol–climate model intercomparison studies, *Atmos. Chem. Phys.*, 14,
1128 8631-8645, doi:10.5194/acp-14-8631-2014, 2014.

1129

1130 Zhang, L. M., Gong, S. L., Padro, J., and Barrie, L.: A size-segregated particle dry
1131 deposition scheme for an atmospheric aerosol module, *Atmos. Environ.*, 35,
1132 549-560, doi:10.1016/S1352-2310(00)00326-5, 2001.

1133

1134 Zhang, Q., Streets, D. G., Carmichael, G. R., He, K. B., Huo, H., Kannari, A., Klimont,
1135 Z., Park, I. S., Reddy, S., Fu, J. S., Chen, D., Duan, L., Lei, Y., Wang, L. T., and
1136 Yao, Z. L.: Asian emissions in 2006 for the NASA INTEX-B mission, *Atmos.*
1137 *Chem. Phys.*, 9, 5131-5153, doi:10.5194/acp-9-5131-2009, 2009.

1138

1139 Zhang, R. H., Li, Q., and Zhang, R. N.: Meteorological conditions for the persistent
1140 severe fog and haze event over eastern China in January 2013, *Sci. China Earth*
1141 *Sci.*, 57(1), 26–35, doi:10.1007/s11430-013-4774-3, 2014.

1142

1143 Zhang, R., Wang, H., Hegg, D. A., Qian, Y., Doherty, S. J., Dang, C., Ma, P.-L.,
1144 Rasch, P. J., and Fu, Q.: Quantifying sources of black carbon in western North
1145 America using observationally based analysis and an emission tagging technique
1146 in the Community Atmosphere Model, *Atmos. Chem. Phys.*, 15, 12805-12822,
1147 doi:10.5194/acp-15-12805-2015, 2015a.

1148

1149 Zhang, R., Wang, H., Qian, Y., Rasch, P. J., Easter, R. C., Ma, P.-L., Singh, B.,
1150 Huang, J., and Fu, Q.: Quantifying sources, transport, deposition, and radiative

1151 forcing of black carbon over the Himalayas and Tibetan Plateau, *Atmos. Chem.*
1152 *Phys.*, 15, 6205-6223, doi:10.5194/acp-15-6205-2015, 2015b.

1153

1154 Zhang, X. Y., Wang, Y. Q., Zhang, X. C., Guo, W., and Gong, S. L.: Carbonaceous
1155 aerosol composition over various regions of China during 2006, *J. Geophys.*
1156 *Res.*, 113, D141111, doi:10.1029/2007JD009525, 2008.

1157

1158 Zhang, X. Y., Wang, Y. Q., Niu, T., Zhang, X. C., Gong, S. L., Zhang, Y. M., and Sun,
1159 J. Y.: Atmospheric aerosol compositions in China: spatial/temporal variability,
1160 chemical signature, regional haze distribution and comparisons with global
1161 aerosols, *Atmos. Chem. Phys.*, 12, 779-799, doi:10.5194/acp-12-779-2012,
1162 2012.

1163

1164 Zhang, Y.-L., Huang, R.-J., El Haddad, I., Ho, K.-F., Cao, J.-J., Han, Y., Zotter, P.,
1165 Bozzetti, C., Daellenbach, K. R., Canonaco, F., Slowik, J. G., Salazar, G.,
1166 Schwikowski, M., Schnelle-Kreis, J., Abbaszade, G., Zimmermann, R.,
1167 Baltensperger, U., Prévôt, A. S. H., and Szidat, S.: Fossil vs. non-fossil sources of
1168 fine carbonaceous aerosols in four Chinese cities during the extreme winter haze
1169 episode of 2013, *Atmos. Chem. Phys.*, 15, 1299-1312,
1170 doi:10.5194/acp-15-1299-2015, 2015.

1171

1172 Zhao, Y., Zhang, J., and Nielsen, C. P.: The effects of recent control policies on
1173 trends in emissions of anthropogenic atmospheric pollutants and CO₂ in China,
1174 *Atmos. Chem. Phys.*, 13, 487-508, doi:10.5194/acp-13-487-2013, 2013.
1175

1176 Zhuang, B. L., Jiang, F., Wang, T. J., Li, S., and Zhu, B.: Investigation on the direct
1177 radiative effect of fossil fuel black-carbon aerosol over China, *Theor. Appl.*
1178 *Climatol.*, 104(3), 301–312, doi:10.1007/s00704-010-0341-4, 2011.
1179

1180 Zhuang, B. L., Liu, Q., Wang, T. J., Yin, C. Q., Li, S., Xie, M., Jiang, F., and Mao, H.
1181 T.: Investigation on semi-direct and indirect climate effects of fossil fuel black
1182 carbon aerosol over China, *Theor. Appl. Climatol.*, 114 (3), 651–672,
1183 doi:10.1007/s00704-013-0862-8, 2013.
1184

1185 Zhuang, B. L., Wang, T. J., Liu, J., Li, S., Xie, M., Yang, X. Q., Fu, C. B., Sun, J. N.,
1186 Yin, C. Q., Liao, J. B., Zhu, J. L., and Zhang, Y.: Continuous measurement of
1187 black carbon aerosol in urban Nanjing of Yangtze River Delta, China, *Atmos.*
1188 *Environ.*, 89, 415–424, doi:10.1016/j.atmosenv.2014.02.052, 2014.
1189
1190
1191
1192

1193 **Figure Captions**

1194

1195 **Figure 1.** (a) Spatial distribution of annual mean total emissions (anthropogenic plus
1196 biomass burning, units: $\text{g C m}^{-2} \text{ yr}^{-1}$) of black carbon (BC) averaged over 2010–2014.
1197 The geographical BC source regions are selected as North China (NC, 109°E –east
1198 boundary, 30° – 41°N), South China (SC, 109°E –east boundary, south boundary–
1199 30°N), Southwest China (SW, 100° – 109°N , south boundary– 32°N), Central-West
1200 China (CW, 100° – 109°N , 32°N –north boundary), Northeast China (NE, 109°E –east
1201 boundary, 41°N –north boundary), Northwest China (NW, west boundary– 100°E ,
1202 36°N –north boundary), and Tibetan Plateau (TP, west boundary– 100°E , south
1203 boundary– 36°N) in China and regions outside of China (RW, rest of the world). (b)
1204 Seasonal mean total emissions (units: Gg C , $\text{Gg} = 10^9\text{g}$) of BC from the seven BC
1205 source regions in China and emissions from rest of East Asia (REA, with China
1206 excluded), South Asia (SAS), Southeast Asia (SEA), and Russia/Belarus/Ukraine
1207 (RBU).

1208

1209 **Figure 2.** Simulated seasonal mean near-surface concentrations (left, units: $\mu\text{g m}^{-3}$)
1210 and column burden (right, units: mg m^{-2}) of BC in December-January-February (DJF),
1211 March-April-May (MAM), June-July-August (JJA), and
1212 September-October-November (SON).

1213

1214 **Figure 3.** Comparisons of observed and modeled seasonal mean (a) near-surface
1215 concentrations (units: $\mu\text{g m}^{-3}$) and (b) aerosol absorption optical depth (AAOD) of BC
1216 in China. Solid lines mark the 1:1 ratios and dashed lines mark the 1:3 and 3:1 ratios.
1217 Observed BC concentrations were taken between 2006 and 2007 at 14 sites of the
1218 China Meteorological Administration (CMA) Atmosphere Watch Network (CAWNET)
1219 (Zhang et al., 2012). Observed AAOD of BC are obtained by removing dust AAOD
1220 from total AAOD at 10 sites of the Aerosol Robotic Network (AERONET) (Holben et
1221 al., 2001), following Bond et al. (2013). The observed AAOD are averaged over years
1222 of 2005–2014 with data available. Correlation coefficient (R) and normalized mean

1223 bias (NMB) between observation and simulation are shown on top left of each panel.
1224 $NMB = 100\% \times \sum(M_i - O_i) / \sum O_i$, where M_i and O_i are the modeled and observed
1225 values at site i , respectively. Site locations are shown in Figure S1a.

1226

1227 **Figure 4.** Spatial distribution of seasonal mean AAOD of total aerosols (left) and
1228 Aerosol Index (AI) derived from Ozone Monitoring Instrument (OMI) measurements
1229 over years of 2010–2014 (right).

1230

1231 **Figure 5.** Spatial distribution of seasonal mean near-surface concentrations of BC
1232 ($\mu\text{g m}^{-3}$) originating from the seven source regions in China (NC, SC, SW, CW, NE,
1233 NW, and TP), marked with black outlines, and sources outside China (RW).
1234 Regionally averaged BC in China contributed by individual source regions is shown at
1235 the bottom right of each panel.

1236

1237 **Figure 6.** Spatial distribution of relative contributions (%) to seasonal mean
1238 near-surface BC concentrations from each of the tagged source regions.

1239

1240 **Figure 7.** Relative contributions (%) from the tagged source regions (denoted by
1241 colors) to regional mean surface concentrations of BC over seven receptor regions in
1242 China (NC, SC, SW, CW, NE, NW, and TP) and China (seven regions combined, CN)
1243 in different seasons. The receptor regions are marked on the horizontal axis in each
1244 panel.

1245

1246 **Figure 8.** Composite differences in winds at 850 hPa (m s^{-1}) and near-surface BC
1247 concentrations ($\mu\text{g m}^{-3}$) between polluted and normal days in DJF.

1248

1249 **Figure 9.** Composite differences in surface BC concentrations ($\mu\text{g m}^{-3}$) averaged
1250 over receptor regions (marked on the horizontal axis) over eastern and central China
1251 between polluted and normal days in DJF originating from individual sources regions
1252 (bars in each column).

1253

1254 **Figure 10.** Spatial distribution of (a, b) column burden (mg m^{-2}) and (c, d)
1255 near-surface concentrations ($\mu\text{g m}^{-3}$) of BC originating from total emissions inside
1256 (CN) and outside China (RW), respectively, in March-April-May (MAM). The black
1257 solid lines over western (150°E , $20^\circ\text{--}60^\circ\text{N}$) Pacific in panel (a) mark the
1258 cross-sections used to quantify outflow of BC from East Asia. The box over western
1259 United States ($125^\circ\text{--}105^\circ\text{W}$, $30^\circ\text{--}50^\circ\text{N}$) in panel (c) is used to quantify BC
1260 concentrations attributed to sources from China.

1261

1262 **Figure 11.** Spatial distribution of annual mean direct radiative forcing of BC (W m^{-2}) at
1263 the top of the atmosphere originating from the tagged BC source regions in China
1264 (NC, SC, SW, CW, NE, NW, and TP) and source outside China (RW). Regionally
1265 averaged forcing in China contributed by individual source regions is shown at the
1266 bottom right of each panel.

1267

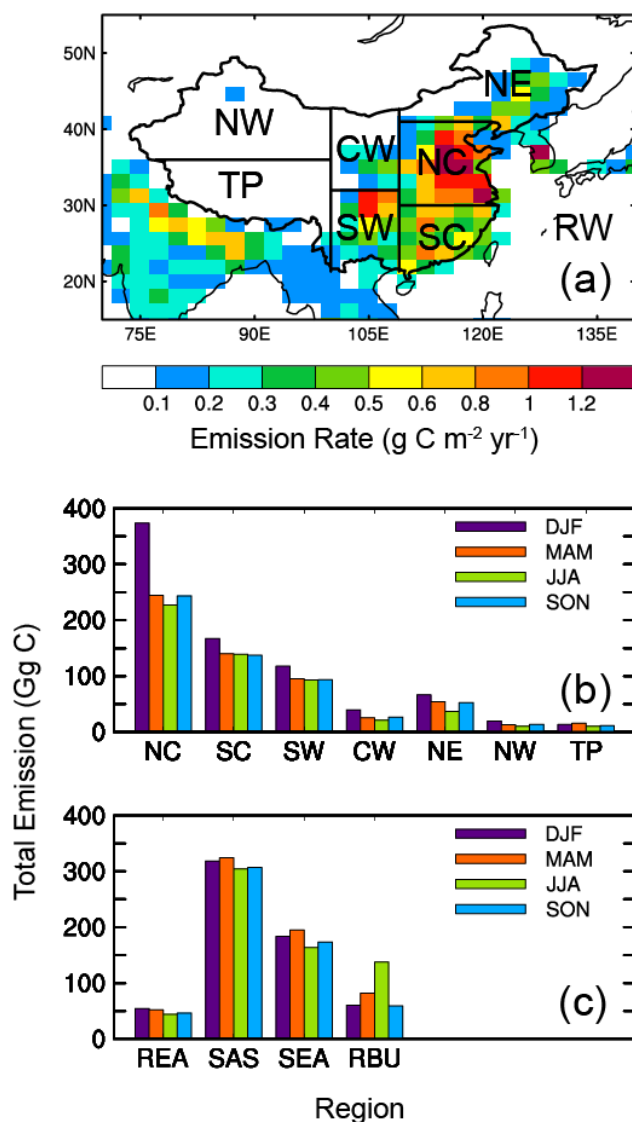
1268 **Figure 12.** (a, c) BC seasonal DRF averaged over China as a function of BC
1269 emission fraction (the ratio of regional emission to the total emission over China and
1270 global, respectively, unit: %) for each of the tagged regions. (b, d) Seasonal DRF
1271 efficiency of BC ($\text{W m}^{-2} \text{Tg}^{-1}$) for each of the tagged source regions over China and
1272 globally, respectively. The efficiency is defined as the DRF divided by the
1273 corresponding scaled annual emission (seasonal emission multiplied by 4). Error bars
1274 indicate $1\text{-}\sigma$ of mean values during years 2010–2014.

1275

1276 **Figure 13.** Seasonal (a, b) near-surface concentration ($\mu\text{g m}^{-3} \text{Tg}^{-1}$) and (c, d) column
1277 burden ($\text{mg m}^{-2} \text{Tg}^{-1}$) efficiency of BC for each of the tagged source regions over
1278 China and globally, respectively.

1279

1280

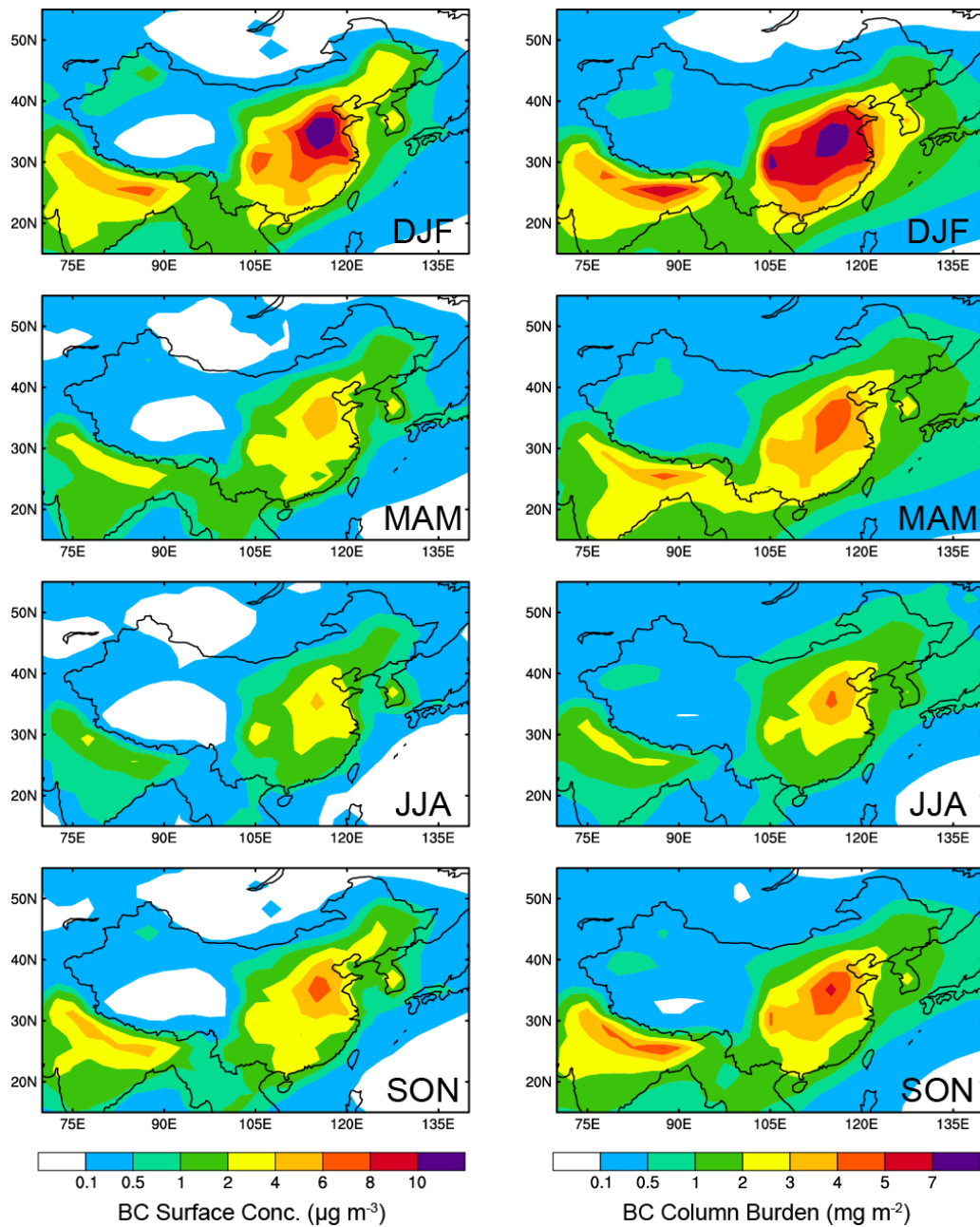


1281

1282

1283 **Figure 1.** (a) Spatial distribution of annual mean total emissions (anthropogenic plus
 1284 biomass burning, units: $\text{g C m}^{-2} \text{ yr}^{-1}$) of black carbon (BC) averaged over 2010–2014.
 1285 The geographical BC source regions are selected as North China (NC, 109°E –east
 1286 boundary, 30° – 41°N), South China (SC, 109°E –east boundary, south boundary–
 1287 30°N), Southwest China (SW, 100° – 109°E , south boundary– 32°N), Central-West
 1288 China (CW, 100° – 109°E , 32°N –north boundary), Northeast China (NE, 109°E –east
 1289 boundary, 41°N –north boundary), Northwest China (NW, west boundary– 100°E ,
 1290 36°N –north boundary), and Tibetan Plateau (TP, west boundary– 100°E , south
 1291 boundary– 36°N) in China and regions outside of China (RW, rest of the world). (b)
 1292 Seasonal mean total emissions (units: Gg C , $\text{Gg} = 10^9\text{g}$) of BC from the seven BC

1293 source regions in China and (c) emissions from rest of East Asia (REA, with China
1294 excluded), South Asia (SAS), Southeast Asia (SEA), and Russia/Belarus/Ukraine
1295 (RBU).



1296

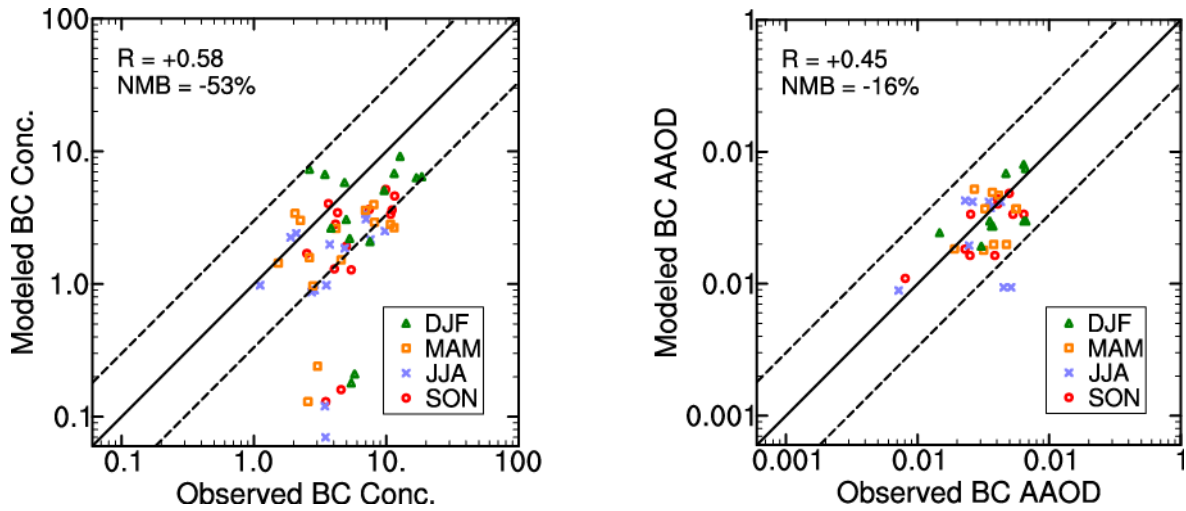
1297

1298 **Figure 2.** Simulated seasonal mean near-surface concentrations (left, units: $\mu\text{g m}^{-3}$)

1299 and column burden (right, units: mg m^{-2}) of BC in December-January-February (DJF),

1300 March-April-May (MAM), June-July-August (JJA), and

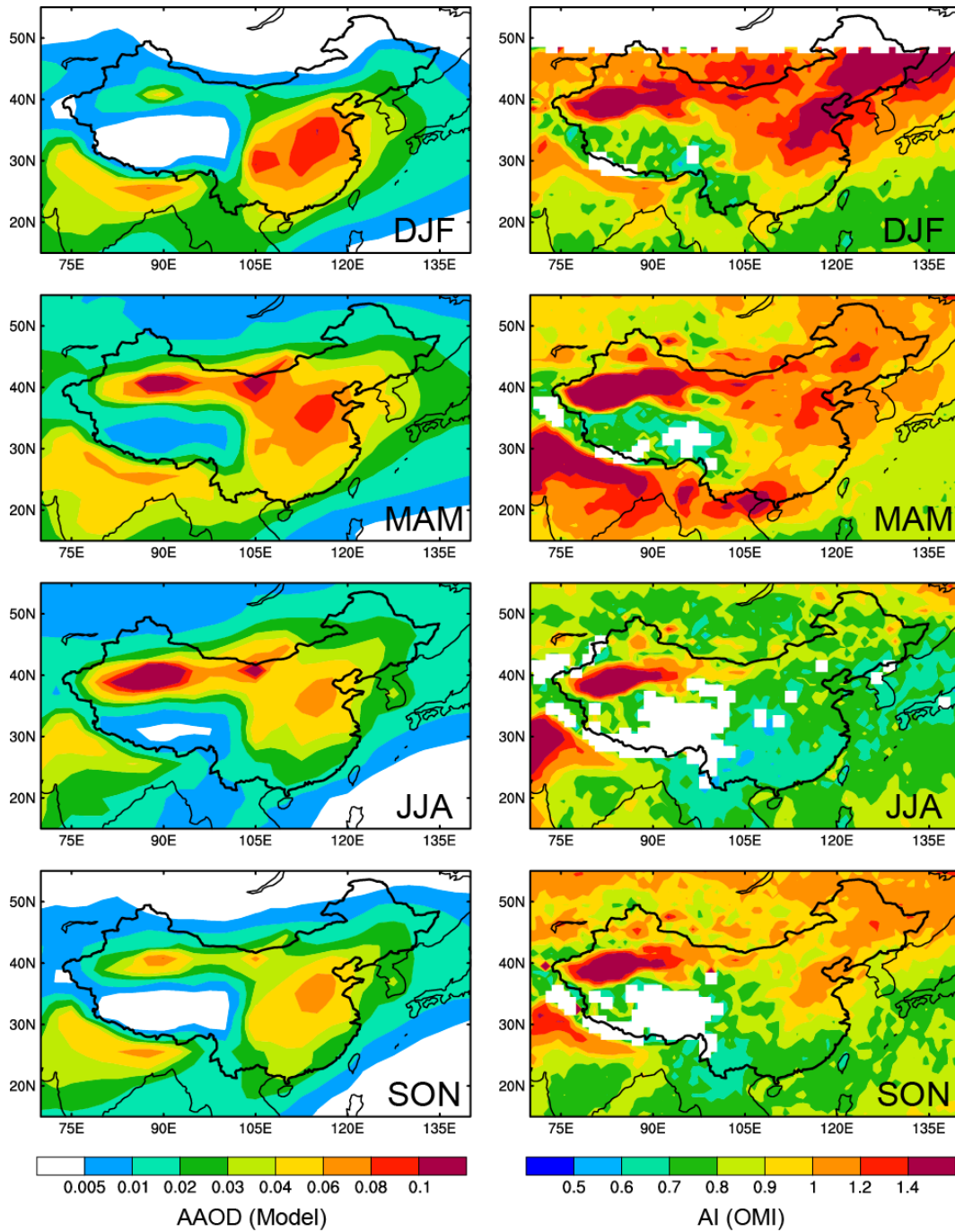
1301 September-October-November (SON).



1302
1303

1304 **Figure 3.** Comparisons of observed and modeled seasonal mean (a) near-surface
1305 concentrations (units: $\mu\text{g m}^{-3}$) and (b) aerosol absorption optical depth (AAOD) of BC
1306 in China. Solid lines mark the 1:1 ratios and dashed lines mark the 1:3 and 3:1 ratios.
1307 Observed BC concentrations were taken between 2006 and 2007 at 14 sites of the
1308 China Meteorological Administration (CMA) Atmosphere Watch Network (CAWNET)
1309 (Zhang et al., 2012). Observed AAOD of BC are obtained by removing dust AAOD
1310 from total AAOD at 10 sites of the Aerosol Robotic Network (AERONET) (Holben et
1311 al., 2001), following Bond et al. (2013). The observed AAOD are averaged over years
1312 of 2010–2014 over 7 sites and 2005–2010 over 3 sites with data available.
1313 Correlation coefficient (R) and normalized mean bias (NMB) between observation
1314 and simulation are shown on top left of each panel. $\text{NMB} = 100\% \times \sum(M_i - O_i) / \sum O_i$,
1315 where M_i and O_i are the modeled and observed values at site i , respectively. Site
1316 locations are shown in Figure S1a.

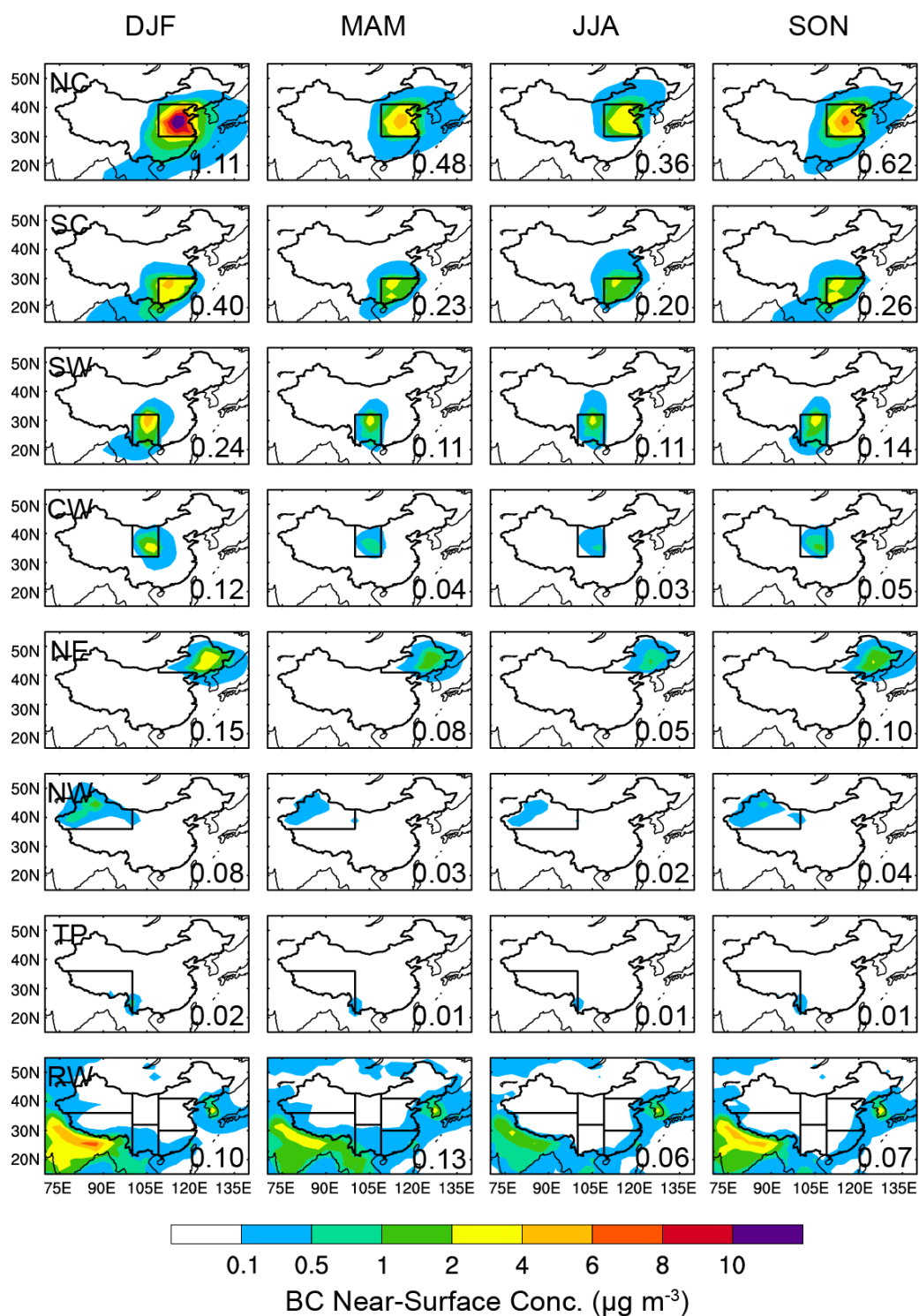
1317
1318



1319

1320

1321 **Figure 4.** Spatial distribution of seasonal mean AAOD of total aerosols (left) and
 1322 Aerosol Index (AI) derived from Ozone Monitoring Instrument (OMI) measurements
 1323 over years of 2010–2014 (right).

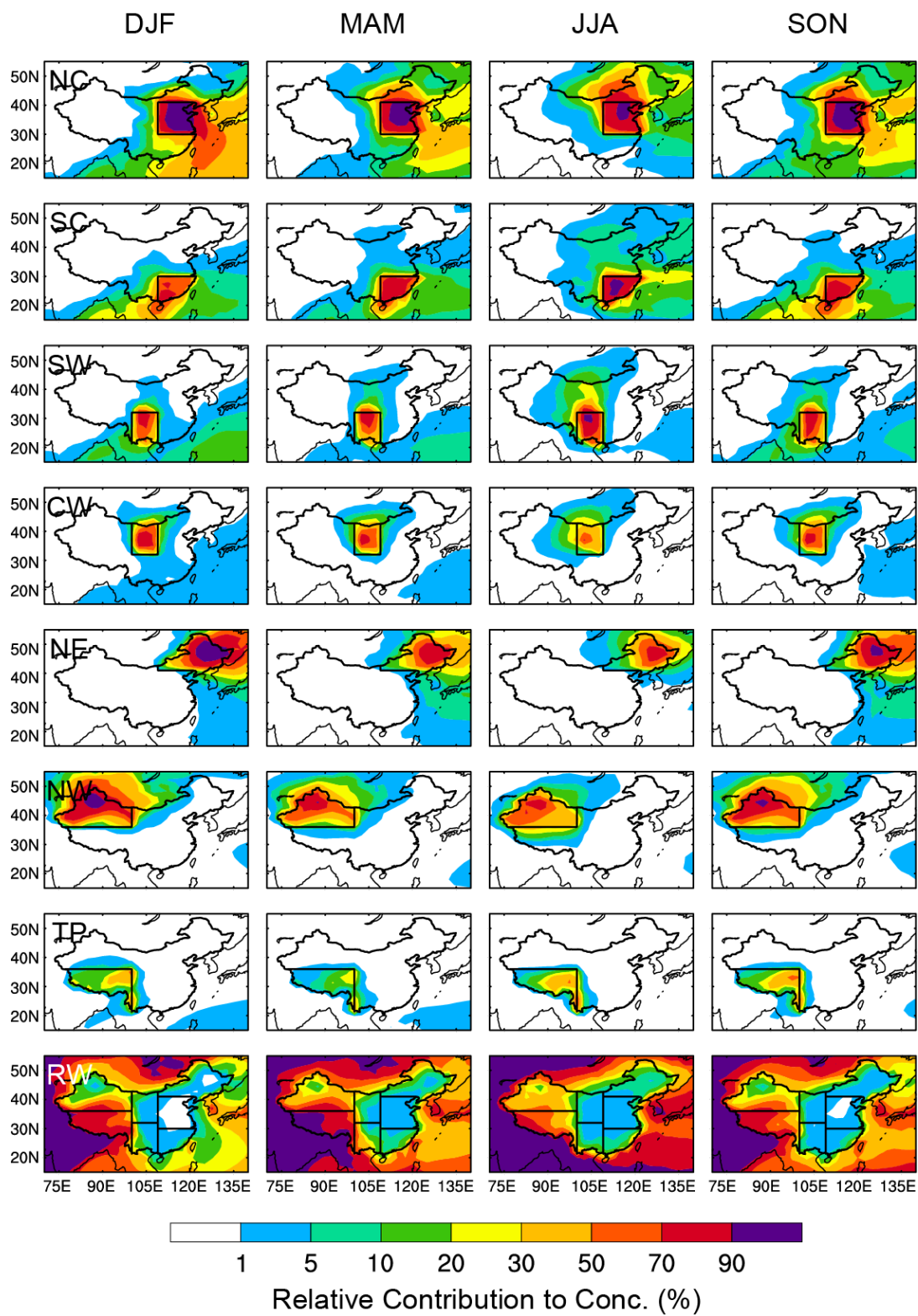


1324

1325

1326 **Figure 5.** Spatial distribution of seasonal mean near-surface concentrations of BC
 1327 ($\mu\text{g m}^{-3}$) originating from the seven source regions in China (NC, SC, SW, CW, NE,
 1328 NW, and TP), marked with black outlines, and sources outside China (RW).

1329 Regionally averaged BC in China contributed by individual source regions is shown at
 1330 the bottom right of each panel.



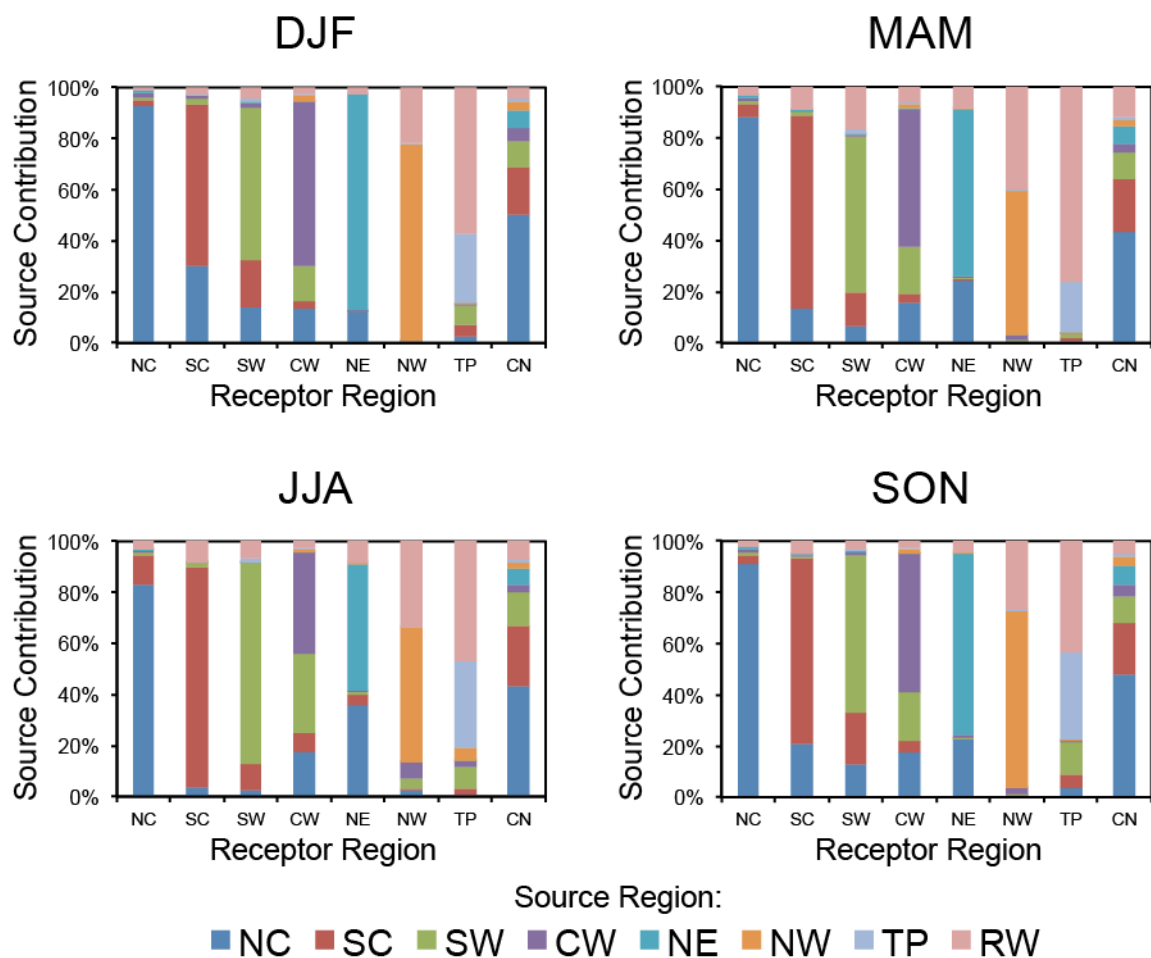
1331

1332

1333 **Figure 6.** Spatial distribution of relative contributions (%) to seasonal mean

1334 near-surface BC concentrations from each of the tagged source regions.

1335



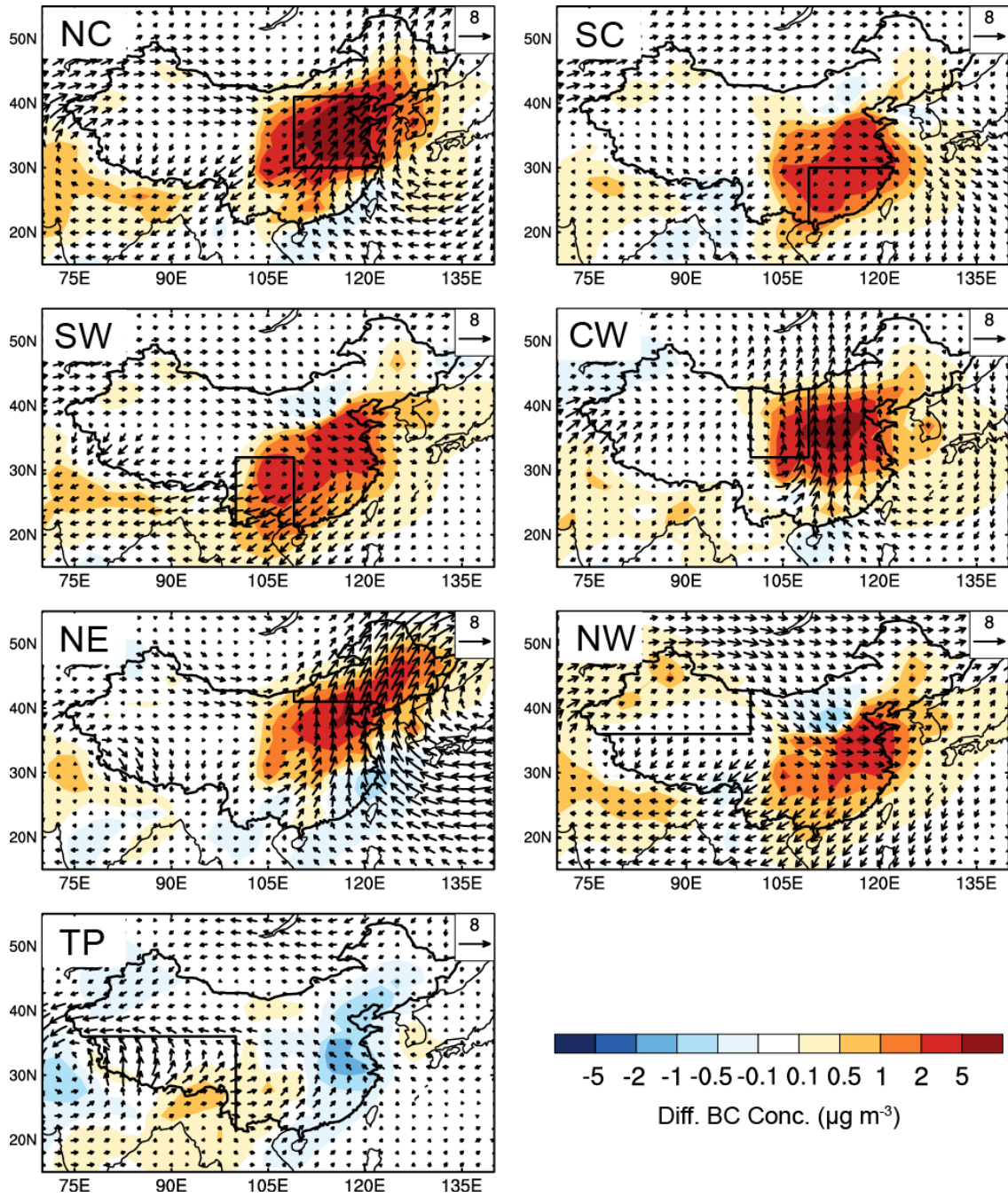
1336

1337

1338 **Figure 7.** Relative contributions (%) from the tagged source regions (denoted by
 1339 colors) to regional mean surface concentrations of BC over seven receptor regions in
 1340 China (NC, SC, SW, CW, NE, NW, and TP) and China (seven regions combined, CN)
 1341 in different seasons. The receptor regions are marked on the horizontal axis in each
 1342 panel.

1343

1344



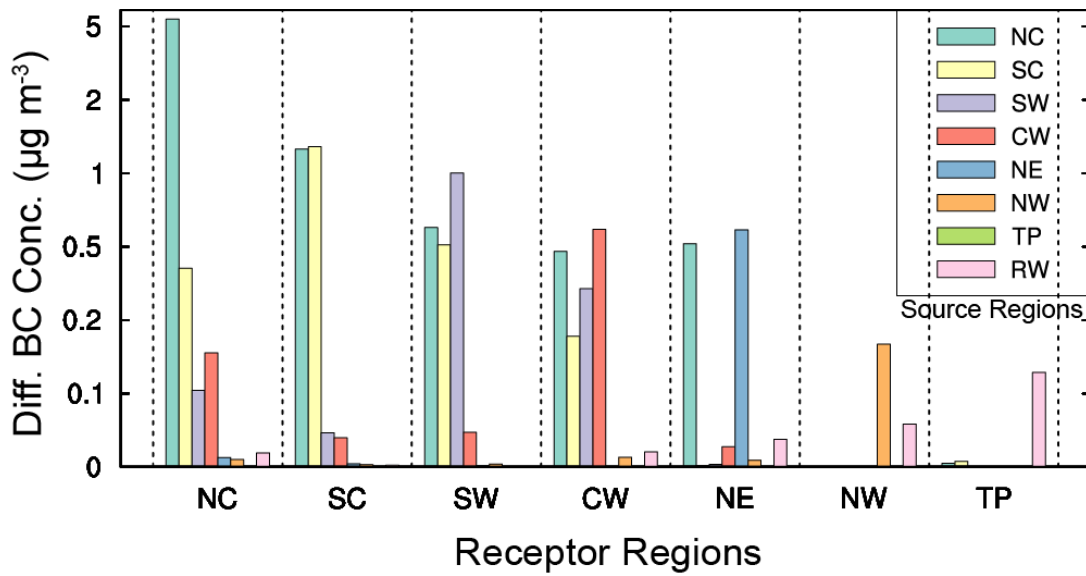
1345

1346

1347 **Figure 8.** Composite differences in winds at 850 hPa (m s^{-1}) and near-surface BC

1348 concentrations ($\mu\text{g m}^{-3}$) between polluted and normal days in DJF.

1349

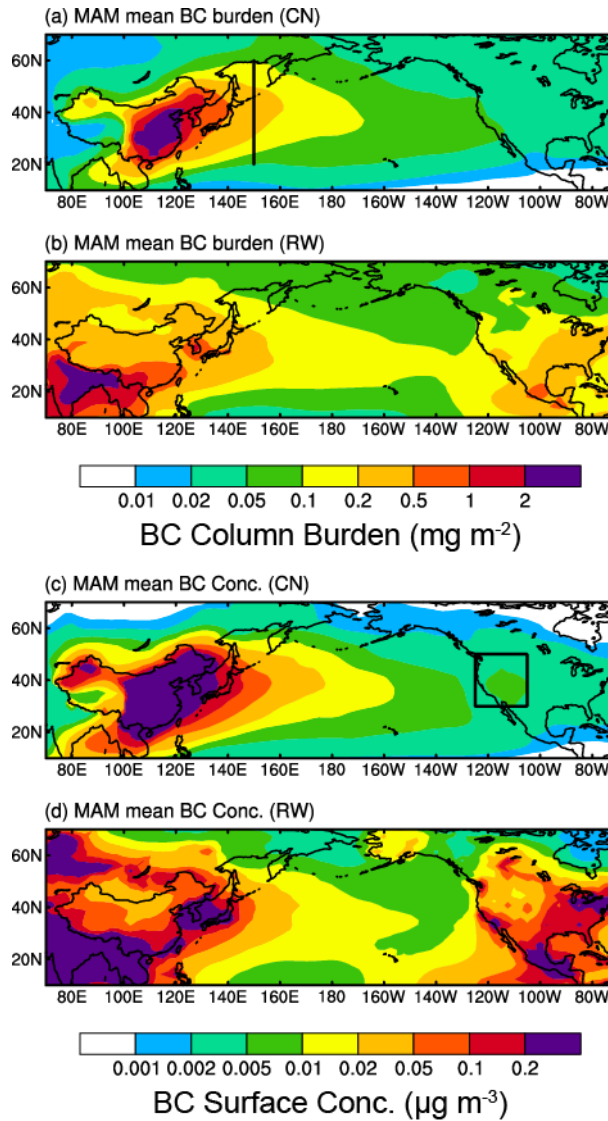


1350

1351

1352 **Figure 9.** Composite differences in surface BC concentrations ($\mu\text{g m}^{-3}$) averaged
 1353 over receptor regions (marked on the horizontal axis) over eastern and central China
 1354 between polluted and normal days in DJF originating from individual sources regions
 1355 (bars in each column).

1356



1357

1358

1359

Figure 10. Spatial distribution of (a, b) column burden (mg m^{-2}) and (c, d)

1360

near-surface concentrations ($\mu\text{g m}^{-3}$) of BC originating from total emissions inside

1361

(CN) and outside China (RW), respectively, in March-April-May (MAM). The black

1362

solid lines over western (150°E , $20^\circ\text{--}60^\circ\text{N}$) Pacific in panel (a) mark the

1363

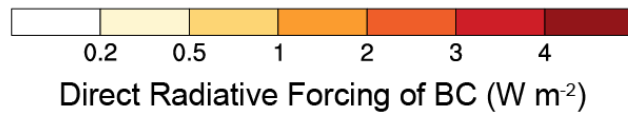
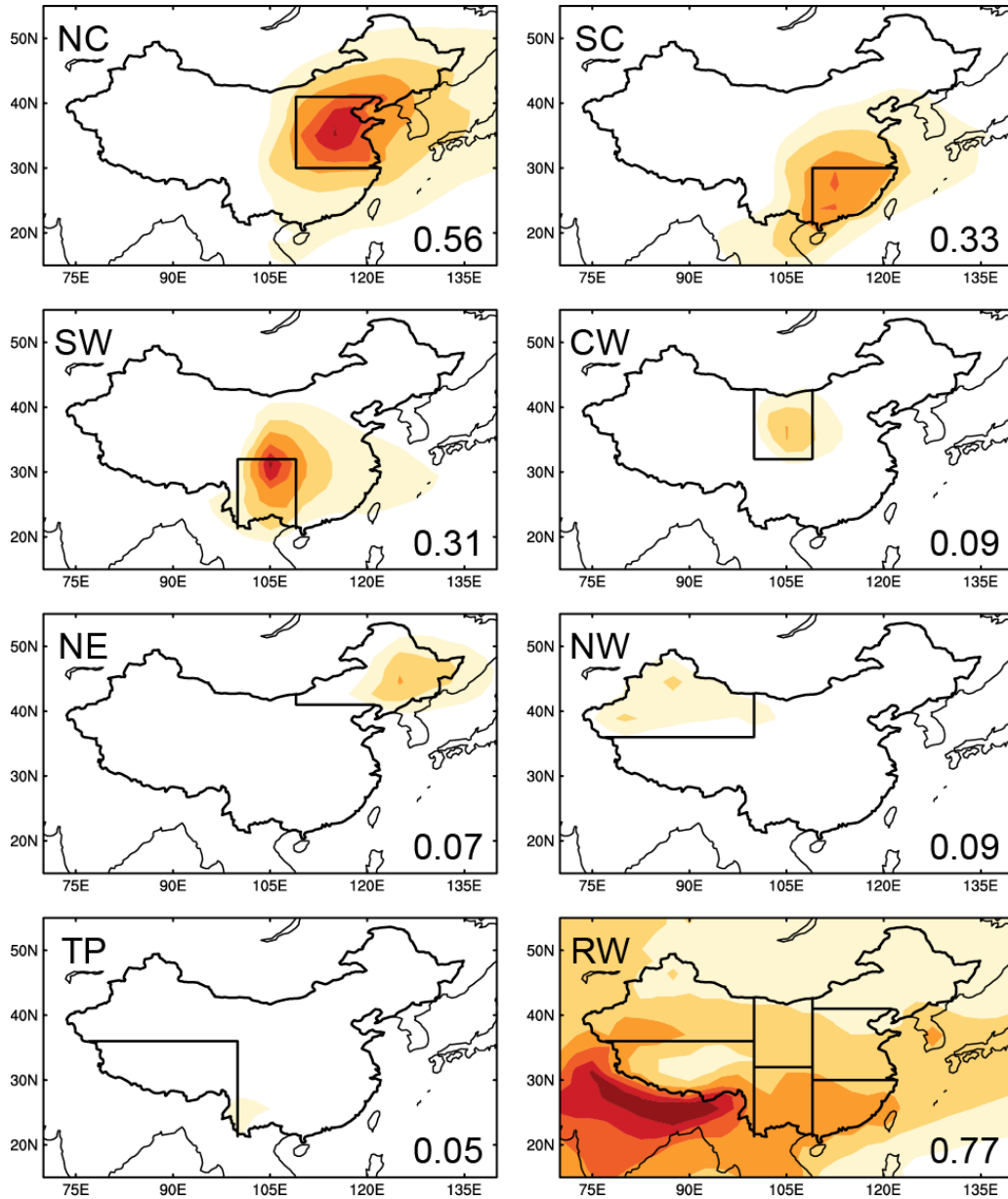
cross-sections used to quantify outflow of BC from East Asia. The box over western

1364

United States ($125^\circ\text{--}105^\circ\text{W}$, $30^\circ\text{--}50^\circ\text{N}$) in panel (c) is used to quantify BC

1365

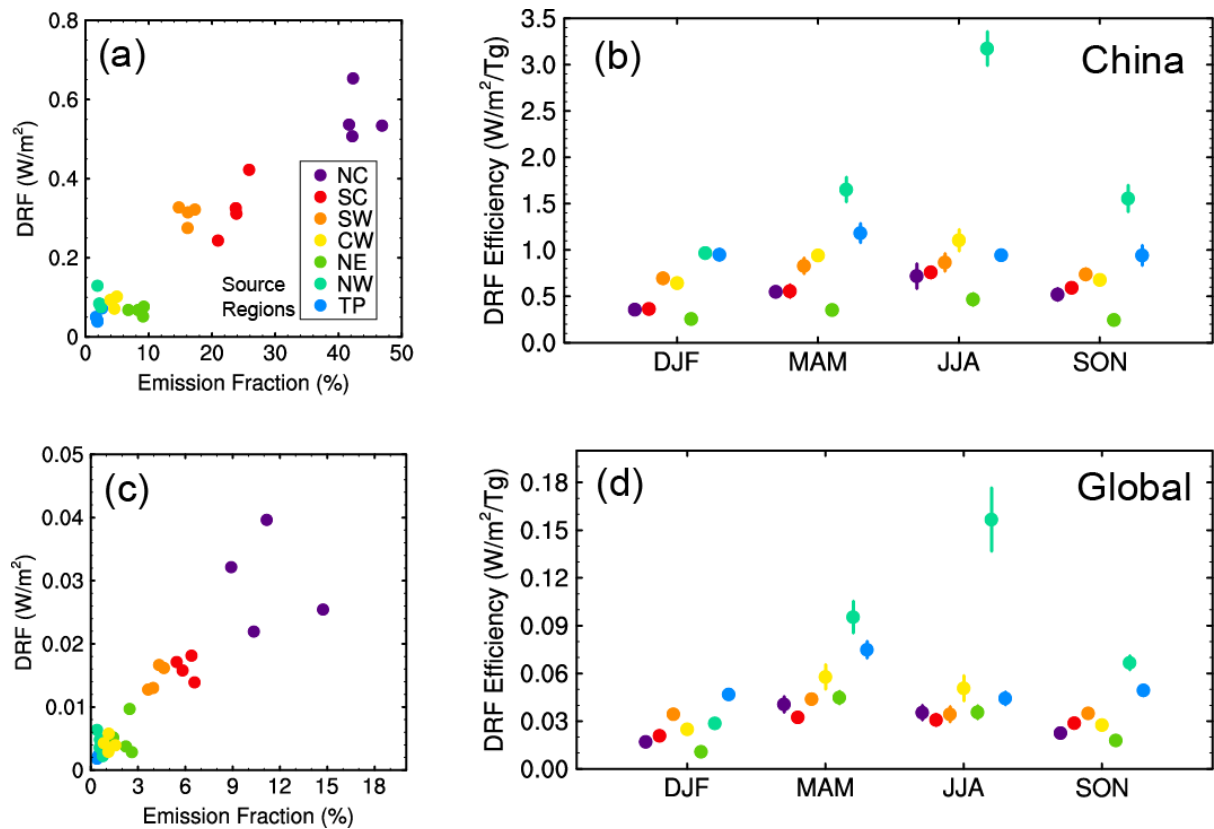
concentrations attributed to sources from China.



1366

1367

1368 **Figure 11.** Spatial distribution of annual mean direct radiative forcing (DRF) of BC (W
 1369 m^{-2}) at the top of the atmosphere originating from the tagged BC source regions in
 1370 China (NC, SC, SW, CW, NE, NW, and TP) and source outside China (RW).
 1371 Regionally averaged forcing in China contributed by individual source regions is
 1372 shown at the bottom right of each panel.



1373

1374

1375 **Figure 12.** (a, c) BC seasonal DRF averaged over China as a function of BC

1376 emission fraction (the ratio of regional emission to the total emission over China and

1377 global, respectively, unit: %) for each of the tagged regions. (b, d) Seasonal DRF

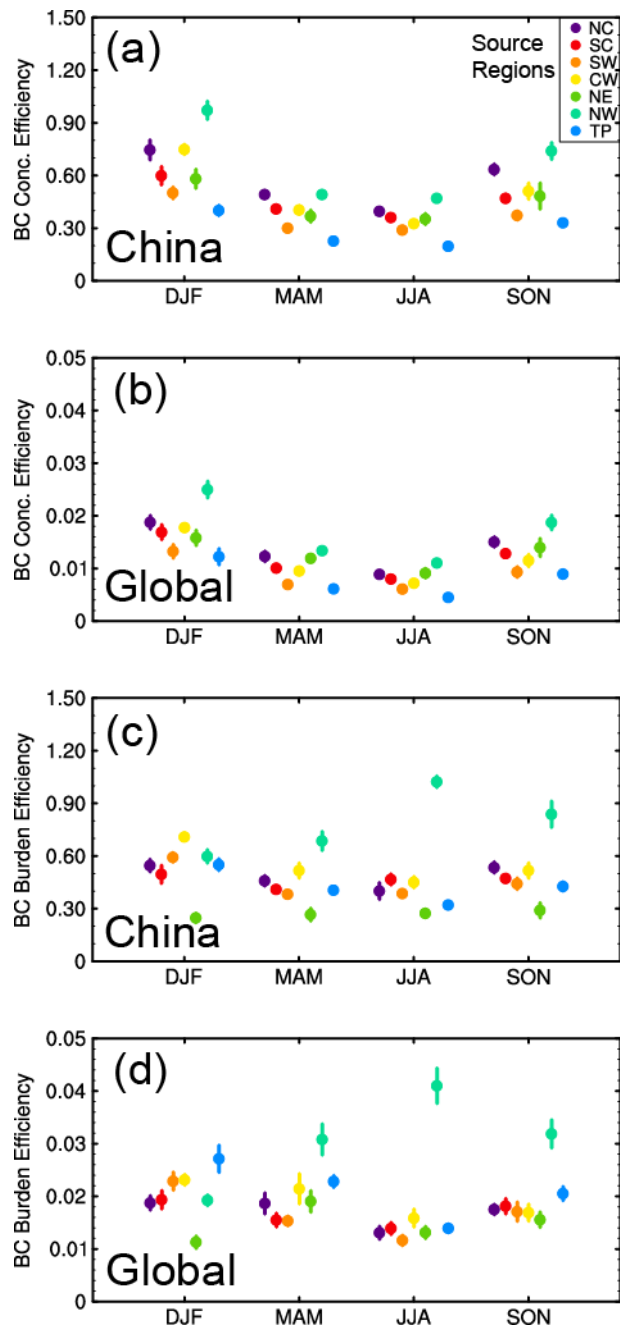
1378 efficiency of BC ($W m^{-2} Tg^{-1}$) for each of the tagged source regions over China and

1379 globally, respectively. The efficiency is defined as the DRF divided by the

1380 corresponding scaled annual emission (seasonal emission multiplied by 4). Error bars

1381 indicate 1- σ of mean values during years 2010–2014.

1382



1383

1384

1385 **Figure 13.** Seasonal (a, b) near-surface concentration ($\mu\text{g m}^{-3} \text{Tg}^{-1}$) and (c, d) column
 1386 burden ($\text{mg m}^{-2} \text{Tg}^{-1}$) efficiency of BC for each of the tagged source regions over
 1387 China and globally, respectively.